

Gain/Loss-free Non-Hermitian Metamaterials

Maopeng Wu,^{1,*} Mingze Weng,^{1,*} Zhonghai Chi,² Yingyi Qi,² Siyong Zheng,²
Fubei Liu,² Xinxin Li,¹ Qian Zhao,^{1,†} Yonggang Meng,¹ and Ji Zhou^{2,‡}

¹*State Key Laboratory of Tribology in Advanced Equipment,*

Department of Mechanical Engineering, Tsinghua University, Beijing 100084, China

²*State Key Laboratory of New Ceramics and Fine Processing,*

School of Materials Science and Engineering, Tsinghua University, Beijing 100084, China

(Dated: August 30, 2024)

Because of the ease of using optical gain or loss, it's widely believed that photonics provides an ideal platform to explore various non-Hermitian (NH) paradigms. Here, without any gain or loss, the non-Bloch wave transport that is unique to NH systems is demonstrated at the junction of the two dimensional Chern insulator and the normal conductor. In the band gap of the non-trivial Chern insulator, the interface between two material types can be effectively described by a one-dimensional NH Hamiltonian—such NH character of the interface is ascribed to the conductor self-energy of a reservoir. As a consequence of asymmetric hopping terms in the interface Hamiltonian, theoretical analysis shows that the wave propagation along the interface exhibits dissipative non-reciprocity (dubbed non-Bloch transport). What's more, this anomaly transport is verified in the junction formed by the electromagnetic metamaterial which is constructed by the reverse-design strategy; the strategy enables the general solution of metamaterial structures for emulating *any* tight-binding models. Further, implementing this strategy, we also investigate the gapless boundary modes in the Haldane-like hyperbolic metamaterial. Our work provides a conceptually rich avenue to construct NH systems for both optics and electronics.

I. INTRODUCTION

Generally, the overall behavior of the open system is mainly extracted from its Hermitian counterpart if we treat the non-Hermitian (NH) part as a perturbation. A crucial lesson learned from recent related investigations is that NH contributions to a system can drastically alter its behavior compared to its Hermitian counterpart. One example of this striking phenomenon is the emergence of exceptional points [1], at which both eigenvalues and their associated eigenvectors coalesce. In a special family of NH Hamiltonians known as parity-time symmetric (or pseudo-Hermitian) systems [2, 3], those peculiar degeneracies are transition points between the symmetric phases, which support entirely real eigenvalue spectra, and the spontaneously broken symmetry phase. In parallel with those developments, the advent of extending topological phases to NH systems reveals a plethora of uniquely NH aspects [4], such as anomalous bulk-boundary correspondence accompanied by the NH skin effect [5–7].

Although the above theoretical explorations originated in the quantum realm, optics and photonics under classical Maxwell's framework have proven to be the ideal experimental platform to observe the rich physics of NH systems [8–11]. This is because they share a similar mathematical structure, despite the distinct physical origins of the two branches of physics. Most importantly, as a consequence of the abundance of nonconservative

processes, photonics provides the essential ingredients to construct NH systems in a controllable manner. Indeed, dissipation can be introduced by the material absorption [12] or the radiation leakage to the surroundings [13]; the optical gain can be implemented through simulated emission [14], which is principal in lasing, or through the parametric processes.

The ease of using optical gain and loss provides such a fertile ground for experimental explorations of NH physics, can we realize a NH optical system involving neither gain nor loss? An affirmative answer is obtained in this work.

Here, we propose the junction between a topological insulator in the non-trivial phase and a conductor for realizing NH systems. This interface has one dimension lower than its constituents, and its effective Hamiltonian consists of (i) the gapless edge state Hermitian Hamiltonian of the topological insulator (ii) and the NH self-energy of the conductor that is considered to be a thermal reservoir. Therefore, the effective junction Hamiltonian is NH even though the total system is Hermitian. To illustrate this idea, we study a junction of the Haldane model coupled with a conductor. We show that this interface Hamiltonian is Hatano-Nelson-like and hopping between lattice sites is non-symmetric, leading to the non-Bloch transmission. Moreover, we discuss the metamaterialization of this junction through a reverse-design strategy; the strategy allows one to determine the electromagnetic metamaterial structure for *any* tight-binding models. The electromagnetic simulation is remarkably consistent with our prediction of non-Bloch transmission. We conclude by considering the outlook for further application in topological states of the hyperbolic lattice. The proposed junction structure together with the reverse-

* These two authors contributed equally.

† zhaopian@tsinghua.edu.cn

‡ zhouji@tsinghua.edu.cn

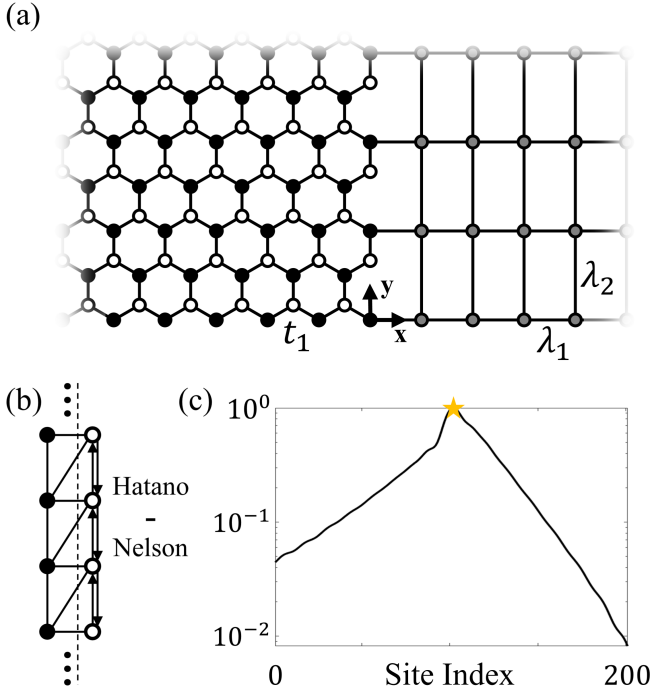


FIG. 1. Junction between the topological insulator (Haldane model) and the conductor. (a) Schematic diagram of the junction. The next-nearest neighbor hopping t_2 is not plotted for simplicity. (b) Effective chain model at the junction around $k_y = 0$. One of the sub-chain is the Hatano-Nelson model. (c) The response profile at the interface corresponding to an excitation (indicated by a star) from Kwant simulation [15]. The different decay rates (left: 0.027, right: 0.043) away from the excitation in the opposite direction suggest the non-Bloch transport.

design strategy extends the scope of the NH photonics.

II. NON-BLOCH TRANSPORT

We consider a two-dimensional Chern insulator (CI) coupled to a conductor, and the line $x = 0$ separates them (see Fig. 1a). The whole system is described by the Hamiltonian $\mathcal{H} = \mathcal{H}_{\text{TI}} + \mathcal{H}_{\text{Cond}} + \mathcal{W}$ with hermiticity

$$\mathcal{H} \rightarrow H_{\text{eff}} = H_{\text{edge}} + \Sigma = \frac{t_1}{2} \begin{pmatrix} \sin \frac{k_y}{2} \\ \frac{1}{2}(1 - e^{-ik_y}) \end{pmatrix} - \frac{1}{2\lambda_1} \begin{pmatrix} \Lambda + \sqrt{-4\lambda_1^2 + \Lambda^2} \\ 0 \end{pmatrix}. \quad (4)$$

where $\Lambda = \mu - \varepsilon + 2\lambda_2 \cos k_y$. Here, we represent H_{eff} in k_y -momentum space by noticing the translation symmetry along y -axis. $H_{\text{edge}} = H_{\text{edge}}^\dagger$ but $\Sigma \neq \Sigma^\dagger$ if $\varepsilon \in \mathbb{B}$ hence the effective Hamiltonian H_{eff} of the interface is NH even though the whole system \mathcal{H} is Hermitian. Note that an extra eigenstate whose eigenvalue is zero appears

$$\mathcal{H} = \mathcal{H}^\dagger.$$

$$\mathcal{H}_{\text{TI}} = t_1 \sum_{\langle i,j \rangle} c_i^\dagger c_j + it_2 \sum_{\langle\langle i,j \rangle\rangle} v_{ij} c_i^\dagger c_j \quad (1)$$

is the Hamiltonian of the Haldane model without breaking the inversion symmetry, t_1 and t_2 are the nearest and next-nearest neighbor hopping of the honeycomb sublattice (let's denote the sublattice as A and B), $v_{ij} = \pm 1$ depending on the vectors along the two bonds. By referring to the phase diagram of the Haldane model, one can find \mathcal{H}_{TI} is in the topological phase and the two bands are separated by $\mathbb{G} \equiv (-3\sqrt{3}t_2, 3\sqrt{3}t_2)$, indicating the topological states in the gap. The Hamiltonian

$$\mathcal{H}_{\text{Cond}} = \lambda_1 \sum_{\langle i,j \rangle_x} a_i^\dagger a_j + \lambda_2 \sum_{\langle i,j \rangle_y} a_i^\dagger a_j + \mu \sum_i a_i^\dagger a_i \quad (2)$$

describes the conductor with its band spanning $\mathbb{B} \equiv [u - 2|\lambda_1| - 2|\lambda_2|, u + 2|\lambda_1| + 2|\lambda_2|]$. μ denotes the on-site energy and $\lambda_{1(2)}$ is the nearest neighbor hopping along $x(y)$ of the square lattice.

$$\mathcal{W} = \lambda_1 \sum_{x_i=1, j \in A \ \& \ x_j=0} a_i^\dagger c_j + h.c. \quad (3)$$

gives the coupling on the interface.

Several cases are rather trivial or well-studied and hence been excluded here: (i) the excitation energy ε is in the conduction bands of CI and the conductor, the transport perpendicular to the interface is much like that between conductors; (ii) the excitation energy is in the conduction band of CI and the band gap of the conductor, the perpendicular transport is blocked; (iii) the energy is in their gaps, it's well known that the transport along the interface is unidirectional and the number of the channel equals the Chern number [16, 17]. We consider the transport parallel to the interface when $\varepsilon \in \mathbb{B} \cap \mathbb{G}$. In that case, \mathcal{H}_{TI} can be reduced to the effective Hamiltonian H_{edge} for the edge states, and the reservoir assumption leads to that the effect of $\mathcal{H}_{\text{Cond}}$ and \mathcal{W} can be replaced by the self-energy Σ of the conductors [18, 19]. That is (more details see Appendix B)

in constructing H_{eff} , we need to drop it in the calculation.

It's very hard to find a tight-binding chain lattice that corresponds to H_{eff} , so to give it an intuition, we consider the approximation model (e.g., $\sin \frac{k_y}{2} \approx \frac{1}{2} \sin k_y$) around $k_y = 0$ and set $t_1 = \lambda_1 = 1$, $\lambda_2 = -1.14$ and $\mu = \varepsilon = 0$.

Correspondingly,

$$[H_{\text{eff}}]_{11} = 2\xi \sin k_y - 2\gamma \cos k_y - 2.12i, \quad (5)$$

where $2\xi = 0.25$ and $2\gamma = 1 - 1.46i$. Figure 1b depicts the approximation tight-binding chain. The complex constant in the equation results in a global dissipation. By inspection, $[H_{\text{eff}}]_{11}$ is nothing but the Hatano-Nelson model [20] describing the vortex pinning in superconductors. The hopping in this model is asymmetric, i.e. $t_{ij} = -i\xi - \gamma$ from site j to i while $t_{ji} = i\xi - \gamma$ from site i to j , and $t_{ij} \neq t_{ji}^*$; it follows that the bulk states pile up at the boundary, namely, the NH skin effect. To describe the dispersion correctly, one needs to generalize $k_y \in \mathbb{R}$ to the complex domain $k_y \in \mathbb{C}$ [5, 21].

The response profile $|\varphi|$ at the interface corresponding to an excitation is an indicator of the non-Bloch transport due to $k_y \in \mathbb{C}$. If the chain eigenenergy $E \in \mathbb{R}$ and $k_y \in \mathbb{C}$, the profile $|\varphi| \propto e^{\alpha y}$, $\alpha \in \mathbb{R}$ because of the skin effect. Inversely, if $E \in \mathbb{C}$ and $k_y \in \mathbb{R}$, $|\varphi| \propto \begin{cases} e^{\beta y}, & y < 0 \\ e^{-\beta y}, & y > 0 \end{cases}$, $\beta \in \mathbb{R}$ due to the dissipation (let the excitation at $y = 0$). Therefore, in general cases, $|\varphi| \sim \begin{cases} e^{(\alpha+\beta)y}, & y < 0 \\ e^{(\alpha-\beta)y}, & y > 0 \end{cases}$. So, the different decay (or growth) rates away from the excitation in the opposite direction indicate the non-Bloch transport.

The non-Bloch wave at the TI-conductor junction is universal. The reason is two-fold: (i) As part of the junction, the TI does not have to be the type of CI. The localized edge states make it possible to construct an effective one-dimensional system through the interface of two-dimensional materials. So, in principle, the CI (class A) used here can be replaced by other types of TI (e.g. class AII). In a separate work [22], we realize the \mathbb{Z}_2 NH skin effect at the interface between a time-reversal TI and a conductor; (ii) In contrast to Ref. [23], no extra requirement for the conductor is adopted here. In there, a relative momentum shift between the reservoir and the nanowire leads to asymmetric hopping. However, this asymmetry in our model results from the interaction between the unidirectional topological states and the reservoir self-energy.

III. POSSIBLE REALIZATION UNDER REVERSE DESIGN

For the normal design procedure of topological metamaterials, one starts with some necessary parameters, such as lattice parameters, material parameters, unit cell structure, and so on; with those parameters, the dispersion relation of the metamaterials can be calculated with the help of the finite element simulation; if the band from the simulation is not topological, we tune the parameters and start over. That iterative procedure costs a huge of computing resources because of lack of generality, and the design may pose a challenge to sample fabrication (e.g.,

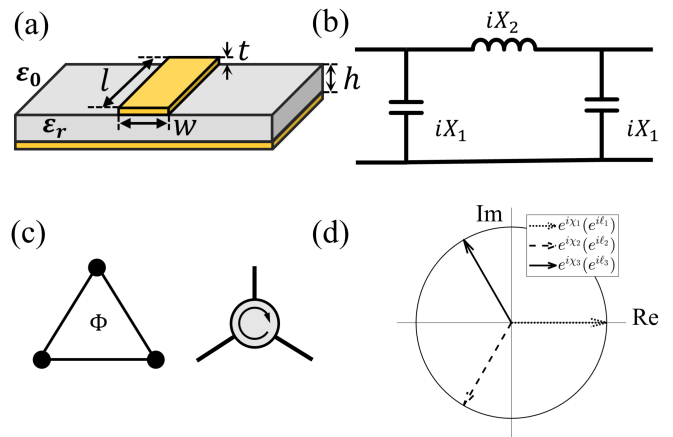


FIG. 2. Principle of the reverse design and introducing non-reciprocal hopping t_2 . (a) Schematic diagram of microstrip waveguide. $w = 2.1$ mm, $h = 1.2$ mm, $\epsilon_r = 4.6$ lead to the characteristic impedance $Z_0 = 50\Omega$ at 2.4 GHz. (b) Π -shape equivalent lumped circuit model of the microstrip, where $X_1 = \frac{1}{Z_0} \tan \frac{kl}{2}$ and $X_2 = -\frac{1}{Z_0 \sin kl}$ with k being the wavenumber of the waveguide. (c) Equivalent connectivity between the Δ -configuration of the three-site model and the Y-configuration of a circulator, and their characteristics (d) when $\Phi = \frac{3\pi}{2}$.

[24]). The starting point of the reverse design proposed here is the tight-binding model, and in principle, the design does not need the aid of finite element simulation. As a proof of concept, we illustrate this idea by realizing the junction mentioned above in the S band (2 – 4 GHz) range, and the design scheme is readily generalized to the optical range.

First, consider the \mathcal{H}_{TI} of Eq. 1 when $t_2 = 0$ (i.e., a graphene model). Implementing temporal topoelectrical circuit (TTC) theory [25, 26], we can construct a circuit lattice with those correspondences, Hamiltonian $\mathcal{H} \leftrightarrow$ admittance Y , eigenvalues $E \leftrightarrow$ self-admittance Y_0 . The spirit of reverse design is that a waveguide with length (e.g., a microstrip line in Fig. 2a) is equivalent to a lumped circuit model (Fig. 2b). This equivalence enables one to ‘update’ a circuit lattice to a metamaterial in wave systems very effectively. More details about design including the graphene circuit, the converted waveguide metamaterial and its optimization can be found in Appendix F. Compared to the existing topoelectrical circuits [27, 28], TTC is more suitable to be the starting point of the reverse design, because the impedance measurements required by existing circuits are out of reach in scattering experiments while scattering measurements are more accessible for electromagnetic metamaterials.

Next, we show how to introduce the next neighbor T-breaking hopping t_2 of \mathcal{H}_{TI} which is critical to the Haldane model. It’s well-known this T-breaking term can be realized by nonreciprocal devices [29–32], e.g., a RF circulator. In reality, a nonreciprocal device has very limited bandwidth, for example, the typical bandwidth is a few hundreds MHz for a RF circulator working at GHz,

thus the frequency range of resonant-based metamaterials emulating the tight-binding Haldane model should be in this bandwidth. This frequency concern should not bother us since our TTC or TTC-based design operates at a fixed frequency and is not resonance-based. According to our previous works [25, 26], it looks like introducing the hopping t_2 can be easily achieved by finding out the admittance of the RF circulator, however, in general, the circulator does not have a well-defined admittance (Part 1 in Appendix E).

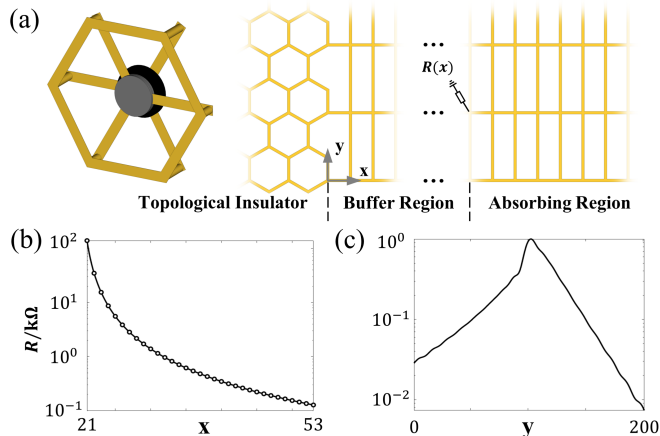


FIG. 3. Metamaterial realization of non-Bloch transport under reverse design. (a) Metamaterial junction consisting of microstrip lines. The left inset, where substrates are not plotted for clarity, shows the non-reciprocal coupling t_2 using the three-port circulator. In absorbing region, the complex potentials are realized by grounding all nodes with resistances (only one grounded node is plotted). (b) The grounding resistances $R(x)$ varies as x . (c) The electric response profile at the interface from CST simulation at 2.4 GHz, indicating the non-Bloch transport.

To solve that, let's first understand the hopping in a geometric manner. Without loss of generality, we consider a minimal model containing three identical sites with hopping t_2 connecting them. The flux Φ in the plaquette leads to a phase θ in t_2 , and the Hamiltonian is $\mathcal{H}_\Delta/t_2 = (\Lambda_1 + \Lambda_4 + \Lambda_6) \cos \theta + (\Lambda_2 - \Lambda_5 + \Lambda_7) \sin \theta$ where Λ_i are the Gell-Mann matrices. When $\Phi = 0$, \mathcal{H}_Δ respects D3h symmetry, thus it has two-fold degeneracy eigenvalues. When pumping the flux, the symmetry is lifted down to C3, resulting in the splitting of the degeneracy (note that when $\Phi = n\pi$ with $n \in \mathbb{Z}$, \mathcal{H}_Δ respects D3h up to a gauge). So, we can use the frame of $\mathbf{u} = (\mathbf{v}_1, \mathbf{v}_2, \mathbf{v}_3)$, $\mathbf{v}_1 = (1, 1, 1)^T$, $\mathbf{v}_2 = (1, \alpha, \alpha^2)^T$, $\mathbf{v}_3 = (1, \alpha^2, \alpha)^T$ with $\alpha = e^{\frac{2\pi i}{3}}$. Performing a bilinear transform, we have $\mathcal{S} = \frac{i + \mathcal{H}_\Delta}{i - \mathcal{H}_\Delta}$. \mathcal{S} is unitary: $\mathcal{S}\mathcal{S}^\dagger = 1$, and $\mathbf{u}^{-1}\mathcal{S}\mathbf{u} = \text{diag}(e^{i\chi_1}, e^{i\chi_2}, e^{i\chi_3})$. So, in the frame of \mathbf{u} , characteristics $\chi_{1,2,3}$ uniquely specify the hopping relation between the sites (see Fig. 2d). On the other hand, compared to the admittance, the scattering-parameter of a circulator is always well-defined. In Appendix E, we demonstrate that three similar characteristics (ℓ_1, ℓ_2, ℓ_3)

in a circulator uniquely determine the connectivity of the three nodes; this gives us an correspondence of T-breaking hopping between tight-binding models and the metamaterials (Fig. 2c): $\chi_i \leftrightarrow \ell_i$. In Appendix F, the simulation result establishes that the topological metamaterial designed under this correspondence supports the unidirectional edge state just as the Haldane model does.

Last, in the model of \mathcal{H} , we assume that the size of the conductor $\mathcal{H}_{\text{Cond}}$ is semi-infinite such that it serves as a reservoir. The metamaterial construction of $\mathcal{H}_{\text{Cond}}$ is similar to that of \mathcal{H}_{TI} when $t_2 = 0$, but it's very cumbersome to prepare the sample in that size. Instead, one can reduce the semi-infinite geometry to a finite lattice with proper boundary condition, i.e., the perfect absorbing boundary condition using power-growth complex onsite potentials that completely absorb the incident wave (see Appendix G). The complex potentials are realized by grounding the nodes with resistances (see Fig. 3b). We remark that the boundary complex potential is not the origin of non-Bloch transport and the semi-infinite argument may also be mitigated by a fairly large lattice.

Figure 3a shows the final RF design of the junction with microstrip lines, and Fig. 3c gives the electric field profile with respect to an excitation (from CST simulation). Clearly, the metamaterial junction exhibits the property of the non-Bloch transport which is consistent with the prediction.

IV. OUTLOOKS

To show the great universality of the reverse design, we would like to discuss its application in the hyperbolic lattice. Different from the normal lattice in the flat space or Euclidean space, the hyperbolic space [33–36] is a tiling of the curved space with constant negative curvature. The curvature leads to the separated dimensions of position and momentum space, e.g., the $\{8, 3\}$ tiling (in Schläfli notation) of the two-dimensional curved space has a four-dimensional Brillouin zone. This disagreement promises the band structure richer physics, such as non-Abelian Bloch states [36] and topological phases [37]. Systems in the negatively curved space seem impossible to realize experimentally since the curved space can not be embedded in flat laboratory space. However, some works point out that electric circuits or waveguide resonators with the graph property can overcome this difficulty since the tight-binding models in the hyperbolic space only care about the nodes and the connectivity between nodes. However, there are still some obstacles for waveguide resonators, e.g., how to induce the model-requisite flux in broadband, and one may face a layout problem when two waveguides have to cross over each other.

Figure 4c illustrates the Haldane-like model with $\{8, 3\}$ tiling in hyperbolic space. We set flux $\Phi = 2\pi$ piercing the plaquette (Fig. 4a) formed by four sites hence $(\chi_0, \chi_{+1}, \chi_{-1}, \chi_2) = (0, 0.7048\pi, -0.7048\pi, 0)$. Two

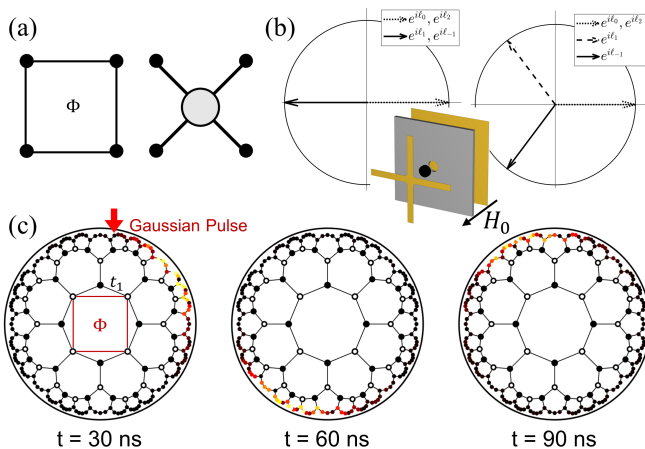


FIG. 4. Introducing nonreciprocal hopping in hyperbolic space and topological edge state of hyperbolic Haldane lattice. (a) Equivalent connectivity between the \square -configuration of the Four-site model and the \times -configuration of a four-port non-reciprocal device. (b) Characteristic adjustment of the ferrite device (inset) by applying external static magnetic field H_0 . Left: characteristics (at disk resonant frequency) when $H_0 = 0$. Right: characteristics corresponding to $\Phi = \pi$ when $H_0 \neq 0$. ℓ_{\pm} are split when $H_0 \neq 0$. $\varepsilon_f = 25$, $4\pi M_s = 1800$ Gauss, $\Delta H = 18$ Oe, and the radius of the ferrite disk (in black) is 2 mm. H_0 affects the relative permeability tensor, so we only keep track of S-parameter at its resonant frequency at GHz. (c) Time-evolution of an electric wave packet on the boundary of the hyperbolic Haldane lattice at 8.24 GHz. We omit the most of next-neighbor hoppings for simplicity.

steps are taken to emulate the flux (Fig. 4b inset): (i) varying the ferrite diameter so that the unmagnetized disk resonates under $HE_{\pm 1,1,1}$ eigenmodes. The $HE_{\pm 1,1,1}$ field patterns lead to $(\ell_0, \ell_{+1}, \ell_{-1}, \ell_2) = (0, -1, -1, 0)$ (Fig.4b left); (ii) applying a magnetic field B_0 will rotate $\ell_{\pm 1}$ in opposite directions while retaining the accidental degeneracy $\ell_{0,2} = 0$ (Fig.4b right). More details see Appendix E.5. Note that the device is *not* a four-port circulator. Bending the waveguide or increasing its physical length will not change its equivalent circuit as long as its electrical length is fixed. Above flexibility makes it possible to construct hyperbolic lattices on Euclidean substrates. The chiral edge state of the model is confirmed through the time evolution of a wave packet propagating clockwise along the boundary.

In summary, we provide an alternate approach to realize non-Hermitian systems in electromagnetics in a gain-free fashion. The reverse design procedure, i.e., the tight-binding models \rightarrow temporal topological circuits \rightarrow electromagnetic metamaterials, offers a prevalent paradigm to design the topological band of the metamaterials.

ACKNOWLEDGMENTS

We wish to acknowledge the support of the National Key Research & Development Program of China (Grant No.2023YFB3811400), National Natural Science Foundation of China (No. 52273296 and No. 51872154), Beijing Municipal Science & Technology Commission (No. Z221100006722016).

-
- [1] M.-A. Miri and A. Alu, Exceptional points in optics and photonics, *Science* **363**, eaar7709 (2019).
 - [2] C. M. Bender, Making sense of non-hermitian hamiltonians, *Reports on Progress in Physics* **70**, 947 (2007).
 - [3] A. Mostafazadeh, Pseudo-Hermiticity versus PT symmetry: The necessary condition for the reality of the spectrum of a non-Hermitian Hamiltonian, *Journal of Mathematical Physics* **43**, 205 (2002).
 - [4] E. J. Bergholtz, J. C. Budich, and F. K. Kunst, Exceptional topology of non-hermitian systems, *Rev. Mod. Phys.* **93**, 015005 (2021).
 - [5] S. Yao and Z. Wang, Edge states and topological invariants of non-hermitian systems, *Phys. Rev. Lett.* **121**, 086803 (2018).
 - [6] F. K. Kunst, E. Edvardsson, J. C. Budich, and E. J. Bergholtz, Biorthogonal bulk-boundary correspondence in non-hermitian systems, *Phys. Rev. Lett.* **121**, 026808 (2018).
 - [7] K. Zhang, Z. Yang, and C. Fang, Correspondence between winding numbers and skin modes in non-hermitian systems, *Phys. Rev. Lett.* **125**, 126402 (2020).
 - [8] L. Feng, R. El-Ganainy, and L. Ge, Non-hermitian photonics based on parity-time symmetry, *Nature Photonics* **11**, 752 (2017).
 - [9] R. El-Ganainy, K. G. Makris, M. Khajavikhan, Z. H. Musslimani, S. Rotter, and D. N. Christodoulides, Non-hermitian physics and pt symmetry, *Nature Physics* **14**, 11 (2018).
 - [10] V. V. Konotop, J. Yang, and D. A. Zezyulin, Nonlinear waves in \mathcal{PT} -symmetric systems, *Rev. Mod. Phys.* **88**, 035002 (2016).
 - [11] T. Ozawa, H. M. Price, A. Amo, N. Goldman, M. Hafezi, L. Lu, M. C. Rechtsman, D. Schuster, J. Simon, O. Zeitlinger, and I. Carusotto, Topological photonics, *Rev. Mod. Phys.* **91**, 015006 (2019).
 - [12] R. El-Ganainy, K. G. Makris, D. N. Christodoulides, and Z. H. Musslimani, Theory of coupled optical pt-symmetric structures, *Opt. Lett.* **32**, 2632 (2007).
 - [13] B. Zhen, C. W. Hsu, Y. Igarashi, L. Lu, I. Kaminer, A. Pick, S.-L. Chua, J. D. Joannopoulos, and M. Soljačić, Spawning rings of exceptional points out of dirac cones, *Nature* **525**, 354 (2015).
 - [14] C. E. Rüter, K. G. Makris, R. El-Ganainy, D. N. Christodoulides, M. Segev, and D. Kip, Observation of parity-time symmetry in optics, *Nature Physics* **6**, 192 (2010).
 - [15] C. W. Groth, M. Wimmer, A. R. Akhmerov, and X. Waintal, Kwant: a software package for quantum transport, *New Journal of Physics* **16**, 063065 (2014).
 - [16] M. Z. Hasan and C. L. Kane, Colloquium: Topological

- insulators, *Rev. Mod. Phys.* **82**, 3045 (2010).
- [17] X.-L. Qi and S.-C. Zhang, Topological insulators and superconductors, *Rev. Mod. Phys.* **83**, 1057 (2011).
- [18] S. Datta, *Electronic transport in mesoscopic systems* (Cambridge university press, 1997).
- [19] E. J. Bergholtz and J. C. Budich, Non-hermitian weyl physics in topological insulator ferromagnet junctions, *Phys. Rev. Res.* **1**, 012003 (2019).
- [20] N. Hatano and D. R. Nelson, Localization transitions in non-hermitian quantum mechanics, *Phys. Rev. Lett.* **77**, 570 (1996).
- [21] K. Yokomizo and S. Murakami, Non-bloch band theory of non-hermitian systems, *Phys. Rev. Lett.* **123**, 066404 (2019).
- [22] In preparation, .
- [23] H. Geng, J. Y. Wei, M. H. Zou, L. Sheng, W. Chen, and D. Y. Xing, Nonreciprocal charge and spin transport induced by non-hermitian skin effect in mesoscopic heterojunctions, *Phys. Rev. B* **107**, 035306 (2023).
- [24] L. Lu, L. Fu, J. D. Joannopoulos, and M. Soljačić, Weyl points and line nodes in gyroid photonic crystals, *Nature Photonics* **7**, 294 (2013).
- [25] M. Wu, Q. Zhao, L. Kang, M. Weng, Z. Chi, R. Peng, J. Liu, D. H. Werner, Y. Meng, and J. Zhou, Evidencing non-bloch dynamics in temporal topoelectrical circuits, *Phys. Rev. B* **107**, 064307 (2023).
- [26] M. Wu, M. Weng, Z. Chi, Y. Qi, H. Li, Q. Zhao, Y. Meng, and J. Zhou, Observing relative homotopic degeneracy conversions with circuit metamaterials, *Phys. Rev. Lett.* **132**, 016605 (2024).
- [27] C. H. Lee, S. Imhof, C. Berger, F. Bayer, J. Brehm, L. W. Molenkamp, T. Kiessling, and R. Thomale, Topoelectrical circuits, *Communications Physics* **1**, 39 (2018).
- [28] S. Imhof, C. Berger, F. Bayer, J. Brehm, L. W. Molenkamp, T. Kiessling, F. Schindler, C. H. Lee, M. Greiter, T. Neupert, and R. Thomale, Topoelectrical-circuit realization of topological corner modes, *Nature Physics* **14**, 925 (2018).
- [29] Z. Wang, Y. Chong, J. D. Joannopoulos, and M. Soljačić, Observation of unidirectional backscattering-immune topological electromagnetic states, *Nature* **461**, 772 (2009).
- [30] Z. Yang, F. Gao, X. Shi, X. Lin, Z. Gao, Y. Chong, and B. Zhang, Topological acoustics, *Phys. Rev. Lett.* **114**, 114301 (2015).
- [31] T. Hofmann, T. Helbig, C. H. Lee, M. Greiter, and R. Thomale, Chiral voltage propagation and calibration in a topoelectrical chern circuit, *Phys. Rev. Lett.* **122**, 247702 (2019).
- [32] Z. Zhang, P. Delplace, and R. Fleury, Superior robustness of anomalous non-reciprocal topological edge states, *Nature* **598**, 293 (2021).
- [33] A. J. Kollár, M. Fitzpatrick, and A. A. Houck, Hyperbolic lattices in circuit quantum electrodynamics, *Nature* **571**, 45 (2019).
- [34] I. Boettcher, P. Bienias, R. Belyansky, A. J. Kollár, and A. V. Gorshkov, Quantum simulation of hyperbolic space with circuit quantum electrodynamics: From graphs to geometry, *Phys. Rev. A* **102**, 032208 (2020).
- [35] J. Maciejko and S. Rayan, Automorphic bloch theorems for hyperbolic lattices, *Proceedings of the National Academy of Sciences* **119**, e2116869119 (2022).
- [36] P. M. Lenggenhager, J. Maciejko, and T. c. v. Bzdušek, Non-abelian hyperbolic band theory from supercells, *Phys. Rev. Lett.* **131**, 226401 (2023).
- [37] D. M. Urwyler, P. M. Lenggenhager, I. Boettcher, R. Thomale, T. Neupert, and T. c. v. Bzdušek, Hyperbolic topological band insulators, *Phys. Rev. Lett.* **129**, 246402 (2022).
- [38] A. Alase, E. Cobanera, G. Ortiz, and L. Viola, Exact solution of quadratic fermionic hamiltonians for arbitrary boundary conditions, *Phys. Rev. Lett.* **117**, 076804 (2016).
- [39] E. Cobanera, A. Alase, G. Ortiz, and L. Viola, Exact solution of corner-modified banded block-toeplitz eigen-systems, *J. Phys. A: Math. Theor.* **50**, 195204 (2017).
- [40] A. Alase, E. Cobanera, G. Ortiz, and L. Viola, Generalization of bloch's theorem for arbitrary boundary conditions: Theory, *Phys. Rev. B* **96**, 195133 (2017).
- [41] V. Kaladzhyan and C. Bena, Obtaining majorana and other boundary modes from the metamorphosis of impurity-induced states: Exact solutions via the t-matrix, *Phys. Rev. B* **100**, 081106 (2019).
- [42] S. Pinon, V. Kaladzhyan, and C. Bena, Surface green's functions and boundary modes using impurities: Weyl semimetals and topological insulators, *Phys. Rev. B* **101**, 115405 (2020).
- [43] Y. Hatsugai, Chern number and edge states in the integer quantum hall effect, *Phys. Rev. Lett.* **71**, 3697 (1993).
- [44] V. Dwivedi and V. Chua, Of bulk and boundaries: Generalized transfer matrices for tight-binding models, *Phys. Rev. B* **93**, 134304 (2016).
- [45] R. S. K. Mong and V. Shivamoggi, Edge states and the bulk-boundary correspondence in dirac hamiltonians, *Phys. Rev. B* **83**, 125109 (2011).
- [46] M. Wimmer, *Quantum transport in nanostructures: From computational concepts to spintronics in graphene and magnetic tunnel junctions*, Phd thesis, University of Regensburg, Regensburg (2009).
- [47] D. H. Lee and J. D. Joannopoulos, Simple scheme for surface-band calculations. ii. the green's function, *Phys. Rev. B* **23**, 4997 (1981).
- [48] D. Youla, L. Castriota, and H. Carlin, Bounded real scattering matrices and the foundations of linear passive network theory, *IRE Transactions on Circuit Theory* **6**, 102 (1959).
- [49] J. Helszajn, Waveguide and stripline 4-port single-junction circulators (short papers), *IEEE Transactions on Microwave Theory and Techniques* **21**, 630 (1973).
- [50] J. Helszajn, M. McKay, and I. Macfarlane, Complex gyrator circuit of 4-port single junction circulator, *IEEE microwave and wireless components letters* **14**, 40 (2004).
- [51] J. Helszajn, The adjustment of the m-port single-junction circulator, *IEEE Transactions on Microwave Theory and Techniques* **18**, 705 (1970).
- [52] J. Weston and X. Waintal, Linear-scaling source-sink algorithm for simulating time-resolved quantum transport and superconductivity, *Phys. Rev. B* **93**, 134506 (2016).
- [53] T. Kloss, J. Weston, B. Gaury, B. Rossignol, C. Groth, and X. Waintal, Tkwant: a software package for time-dependent quantum transport, *New Journal of Physics* **23**, 023025 (2021).

Appendix A: A review about self-energy

1. Junction

Let us first give the topological junction an intuition. Assuming each side of the junction is described by a Hermitian Hamiltonian, H_0 and H_e , and the two sides are coupled through some surface mechanism, such as the chemical bonds. Then the junction is Hermitian and the total Hamiltonian can be written as.

$$H_J = \begin{pmatrix} H_0 & C \\ C^\dagger & H_e \end{pmatrix}, \quad (\text{A1})$$

where C denotes the coupling. Correspondingly, the retarded green function G_J can be defined as $G_j = (E + i0^+ - H_J)^{-1}$ or

$$G_J = \begin{pmatrix} G_0 & G_{0e} \\ G_{e0} & G_e \end{pmatrix}. \quad (\text{A2})$$

When one of the sides is so ‘‘large’’, say the side described by H_e , that the effect of H_0 on H_e is negligible. In this case, H_e constitutes a reservoir or the environment. After some simple algebra, we can find the Green’s function G_0 of the smaller side is expressed as $G_0 = E + i0^+ - H_0 - \Sigma$, where $\Sigma = C^\dagger G_e^{-1} C$ is the so called self-energy and the effect of H_e on H_0 is encoded with it. So the effective Hamiltonian H_{eff} of the smaller side is $H_{\text{eff}} = H_0 + \Sigma$, and in general H_{eff} is non-Hermitian $H_{\text{eff}} \neq H_{\text{eff}}^\dagger$ owing to the complexity of Σ . Note that the non-Hermiticity is introduced without any gain or loss, while the gain and loss are essential in optical realization. The concept of self-energy is widely applied in physics, such as those coming from the electron-electron/phonon Coulomb interactions, the impurity scattering and the interaction with the reservoir (considered here), although their physical origins may differ.

2. Reservoir argument

In the main article, we realize an effective NH system by considering two coupled subsystems. The self-energy treatment requires that one of the subsystems can be viewed as the reservoir. Here we show that self-energy is out of the capability to delineate two comparable coupled subsystems.

Let’s consider two comparable coupled subsystems with only one state in each (Fig. 5a). The whole system is described by

$$\mathcal{H}_2 = E_1 a^\dagger a + E_2 b^\dagger b + \Omega(a^\dagger b + b^\dagger a), \quad (\text{A3})$$

a^\dagger and a are creation and annihilation operator in subsystem I respectively, b^\dagger and b in subsystem II. Now if we are interested primarily in I, the effect of II through a self-energy is

$$\Sigma_2(\varepsilon) = \frac{\Omega}{\varepsilon - E_1 + i0^+}. \quad (\text{A4})$$

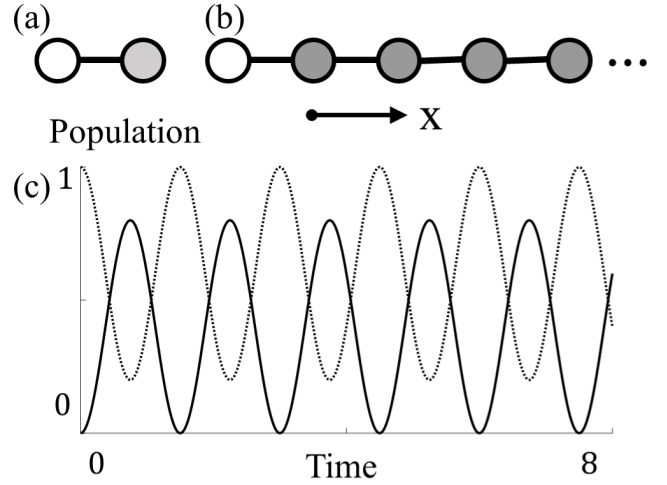


FIG. 5. Reservoir argument. (a) Two comparable coupled subsystems I and II. (b) Two coupled subsystems with the subsystem II consisting of N states. (c) The population dynamics as a function of time in two comparable coupled subsystems. $E_1 = 0$, $E_2 = 1$ and $\Omega = 1$. The solid line represents ρ_{11} and the dot line represents ρ_{22} , the populations present Rabi oscillations.

However, II is not a reservoir in the common sense. The fundamental feature of a reservoir is that the rate constant for outflow or inflow (e.g., heat flow, current flow) remains unaffected by the filling and vacuuming of states and other dynamical details [18]. II does not satisfy this criterion because the escape rate is

$$\gamma_2 = i(\Sigma_2 - \Sigma_2^\dagger) = \frac{\Omega^2 0^+}{(\varepsilon - E_1)^2 + (0^+)^2} \quad (\text{A5})$$

which is affected strongly by 0^+ (a proper reservoir should be independent of 0^+). This means that rate out of I is affected by the rate into it. By using the von-Neumann equation $\frac{d\rho}{dt} = -i[\mathcal{H}_2, \rho]$ we could calculate the populations (ρ_{11}, ρ_{22}) of density matrix ρ as a function of time. The system is then driven between subsystems, and the populations present Rabi oscillations with frequency Ω , as is shown in Fig. 5c.

Now consider two coupled subsystems with the subsystem II consisting of N states (e.g., a chain with N sites, see Fig. 5b), the resulting Hamiltonian is

$$\mathcal{H}_{N+1} = E_1 a^\dagger a + E_2 \sum_i b_i^\dagger b_i + \left[t \sum_i b_i^\dagger b_{i+1} + \Omega a^\dagger b_1 + h.c. \right]. \quad (\text{A6})$$

The eigenenergies of II are given by $\varepsilon_n = E_2 + 2t \cos k_n$ and the corresponding normalized wavefunction is $\phi = \sqrt{\frac{2}{N}} \sin k_n x$, where $k_n = n \frac{\pi}{N}$, $n \in \mathbb{Z}$. So, the effect of II through the self-energy is

$$\Sigma_{N+1}(\varepsilon) = \frac{2}{N} \sum_n \frac{\Omega^2 \sin^2 k_n}{\varepsilon - \varepsilon_n + i0^+}. \quad (\text{A7})$$

When $N \rightarrow \infty$, convert the summation to an integral:

$$\Sigma_\infty = \frac{2}{\pi} \int_0^\pi dk \frac{\Omega^2 \sin^2 k_n}{\varepsilon - \varepsilon_n + i0^+}, \quad (\text{A8})$$

and we have $\Sigma_\infty = \Omega e^{ik}$ (we set $E_1 = E_2$ for simplicity). The escape rate is $\gamma_\infty = i(\Sigma_\infty - \Sigma_\infty^\dagger) = 2\Omega \sin k$. By contrast, the reservoir II with $N \rightarrow \infty$ states has a constant escape rate independent of 0^+ .

Appendix B: Edge state Hamiltonian

There are several ways to calculate the exact solutions of the edge states, such as via extending Bloch's theorem [38–40], the impurity Green's function [41, 42], the transfer matrix [43, 44], the geometric algebra [45] and so on. The difficulty for the Haldane model roots in the next-nearest neighbor hopping. Here, we follow the approach using the Green's function [45]. The calculation is summarized as follows: we begin with a model $h_0(\mathbf{k})$ with fully periodic boundary conditions, which allows us to write down the Hamiltonian in the momentum space; next, we add hopping perturbation $h_1(k_1)$ that substrate the interaction crossing the first row and the end row of the lattice, forming an open boundary along that direction; the final Green's function of the resulting system $h_0 + h_1$ is given by the Dyson equation, and the poles of it enable the analytic solution of the edge states. Note that the geometric algebra method can not be applied here since the next-nearest neighbor hopping appears and the supercell Hamiltonian (e.g., two unit cells) is not of Dirac form.

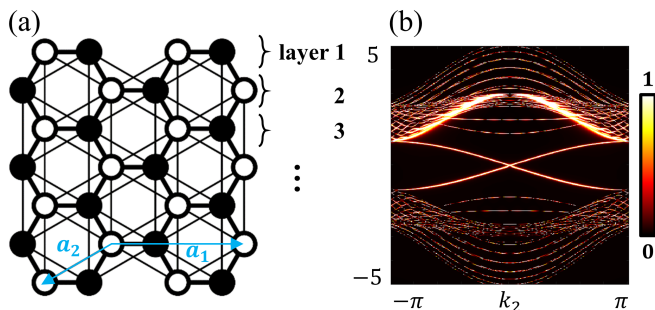


FIG. 6. (a) A semi-infinite two-dimensional honeycomb lattice and a chain of layers. a_1 and a_2 are the lattice unit vectors. We use the non-orthogonal coordinate based on a_1 and a_2 , and reciprocal space (k_1, k_2) corresponds to that coordinate. (b) Local density of states of $G(\varepsilon; k_1, l)$.

1. Green's function with periodic boundaries

After Fourier transform, the Haldane model of Eq. 1 ($t_1 = 1$, Fig. 6a) can be expressed in a compact form as

$h_0(\mathbf{k}) = \mathbf{d} \cdot \boldsymbol{\sigma}$, where

$$\begin{aligned} d_x &= 2t_2 [\sin k_2 + \sin(k_1 + k_2) - \sin(k_1 + 2k_2)], \\ d_y &= 1 + \cos k_2 + \cos(k_1 + k_2), \\ d_z &= -\sin k_2 + \sin(k_1 + k_2). \end{aligned} \quad (\text{B1})$$

And the spectrum of the model is $\varepsilon_{\mathbf{k}} = \pm \sqrt{d_x^2 + d_y^2 + d_z^2}$. Correspondingly, the Green function in \mathbf{k} space is

$$G_0(E; \mathbf{k}) = \frac{1}{\varepsilon - h_0(\mathbf{k})} = \frac{1}{\varepsilon^2 - \varepsilon_{\mathbf{k}}^2} \begin{pmatrix} \varepsilon + d_z & d_x - id_y \\ d_x + id_y & \varepsilon - d_z \end{pmatrix} \quad (\text{B2})$$

To include the hopping perturbation, we keep the momentum coordinate k_1 but perform an inverse Fourier transform to write down the Green's function in real-space coordinate in the a_2 direction. Thus, we have

$$G_0(E; k_1, l) = \begin{pmatrix} g_0 & g_1^\dagger & g_2^\dagger & \cdots & g_2 & g_1 \\ g_1 & g_0 & g_1^\dagger & g_2^\dagger & & \\ g_2 & g_1 & g_0 & g_1^\dagger & & \\ \vdots & g_2 & g_1 & g_0 & & \\ g_2^\dagger & & & & & \\ g_1^\dagger & g_2^\dagger & & & \ddots & \end{pmatrix}_{n,n} \quad (\text{B3})$$

where

$$\begin{aligned} g_0 &= \int \frac{dk_2}{2\pi} G_0(\varepsilon, \mathbf{k}), \\ g_1 &= \int \frac{dk_2}{2\pi} e^{ik_2} G_0(\varepsilon, \mathbf{k}), \\ g_2 &= \int \frac{dk_2}{2\pi} e^{2ik_2} G_0(\varepsilon, \mathbf{k}), \end{aligned} \quad (\text{B4})$$

and $l = ja_2$ with $j = 1, 2, \dots, n$. $G_0(\varepsilon; k_1, l)$ is a n -by- n block matrix.

2. Hopping perturbation

Hopping perturbation $h_1(\varepsilon; k_1, l)$ deletes the hopping crossing the first row and the end row of the lattice, such that it creates two edges perpendicular to a_1 . Its explicit expression is

$$h_1(\varepsilon; k_1, l) = \begin{pmatrix} 0 & \cdots & v_2 & v_1 \\ \vdots & & 0 & v_2 \\ v_2^\dagger & 0 & \ddots & \\ v_1^\dagger & v_2^\dagger & & 0 \end{pmatrix}_{n,n} \quad (\text{B5})$$

where

$$\begin{aligned} v_1 &= \begin{pmatrix} -it_2(1 + e^{ik_1}) & 1 \\ e^{ik_1} & it_2(1 + e^{ik_1}) \end{pmatrix}, \\ v_2 &= \begin{pmatrix} it_2 e^{ik_1} & 0 \\ 0 & it_2 e^{-ik_1} \end{pmatrix} \end{aligned} \quad (\text{B6})$$

$v_1(v_2)$ describes the nearest (next-nearest) neighbor hopping between the layers along a_2 .

3. Green's function with the perturbation

The Dyson equation gives the full Green's function $G(\varepsilon; k_1, l)$ in terms of the initial Green's function

$$(\mathbb{I} - G_0 h_1) \phi = \begin{pmatrix} I - \begin{pmatrix} g_2 & g_1 \\ g_3 & g_2 \end{pmatrix} \begin{pmatrix} v_2 & v_1 \\ 0 & v_2 \end{pmatrix}^\dagger & & & \\ & \ddots & & \\ & & I & \\ & & & I - \begin{pmatrix} g_2 & g_1 \\ g_3 & g_2 \end{pmatrix}^\dagger \begin{pmatrix} v_2 & v_1 \\ 0 & v_2 \end{pmatrix} \end{pmatrix} \begin{pmatrix} u \\ \lambda u \\ \vdots \\ 0 \end{pmatrix} \quad (\text{B8})$$

The ellipses indicate the non-zero subblock. ϕ localizes at the first layer and the $|\lambda| < 1$ promises the localization. And,

$$\begin{aligned} \left[I - \begin{pmatrix} g_2 & g_1 \\ g_3 & g_2 \end{pmatrix} \begin{pmatrix} v_2 & v_1 \\ 0 & v_2 \end{pmatrix}^\dagger \right] \begin{pmatrix} u \\ \lambda u \end{pmatrix} &= 0, \\ \begin{pmatrix} g_0 & g_1^\dagger \\ g_1 & g_0 \end{pmatrix} \begin{pmatrix} v_2 & v_1 \\ 0 & v_2 \end{pmatrix}^\dagger \begin{pmatrix} u \\ \lambda u \end{pmatrix} &= 0, \end{aligned} \quad (\text{B9})$$

which together require (Kramer criterion)

$$\det \begin{pmatrix} g_0 & g_1^\dagger \\ g_1 & g_0 \end{pmatrix} = 0. \quad (\text{B10})$$

It can be further simplified by a decomposition in terms of triangular matrices (note that $\det(g_0) \neq 0$),

$$\begin{aligned} \det \begin{pmatrix} g_0 & g_1^\dagger \\ g_1 & g_0 \end{pmatrix} &= \det \left[\begin{pmatrix} g_0 & 0 \\ g_1 & I \end{pmatrix} \begin{pmatrix} I & g_0^{-1} g_1^\dagger \\ 0 & g_0 - g_1 g_0^{-1} g_1^\dagger \end{pmatrix} \right] \\ &= \det(g_0) \det(g_0 - g_1 g_0^{-1} g_1^\dagger) \end{aligned} \quad (\text{B11})$$

So, we can calculate the edge state spectrum explicitly by solving $\det(g_0 - g_1 g_0^{-1} g_1^\dagger) = 0$. The edge states energy is given by $\varepsilon_\pm(k_1) = \pm \sin(k_1/2)$ with $\varepsilon \in \mathbb{G}$, and $+$ ($-$) corresponds to the state localized at the first (last) layer.

4. Edge state wave vector

We can also calculate the u through Eq. B9. A more convenient method is by extending Bloch's theorem. In

$G_0(\varepsilon; k_1, l)$ and the hopping perturbation h_1 , that is

$$G(\varepsilon; k_1, l) = \frac{G_0}{1 - G_0 h_1}. \quad (\text{B7})$$

The G_0 has no poles in the gap, so the poles of G , alternatively the zeros of $\det(1 - G_0 h_1)$, are the edge state eigenvalues when $\varepsilon \in \mathbb{G}$. To show that, we numerically calculate the local density of states given in general by $n(\varepsilon; k_1) = -\frac{1}{\pi} \text{Im}[\text{tr}G(\varepsilon; k_1, l)]$ (see Fig. 6b). Taking the ansatz of edge state wave vector $\phi = (u, \lambda u, \lambda^2 u, \dots, 0)_{1,n}^\text{T}$ and substituting B3 and B5 into B7, we have

our case, we extend the k_2 to the complex domain \mathbb{C} with an analytic continuation, and we have $h_0(k_1, k_2)u = \varepsilon_+(k_1)u$ with $k_2 \rightarrow k_2' \in \mathbb{C}$. Then the secular equation gives $\det[\varepsilon_+ - h_0(k_1, k_2')] = 0$. With k_2' , u has the form

$$u = \begin{pmatrix} 1 \\ \frac{\varepsilon_+ - d_3(k_2')}{d_1(k_2') - i d_2(k_2')} \end{pmatrix} \quad (\text{B12})$$

where the argument k_1 is suppressed. The normalized solution to this equation is $u = \frac{1}{\sqrt{2}} \left(1, e^{-i \frac{k_1 - \pi}{2}} \right)^\text{T}$.

Finally, we can use the edge state projector uu^\dagger to construct the effective edge Hamiltonian

$$H_{\text{edge}} = \varepsilon_+ uu^\dagger = \frac{1}{2} \begin{pmatrix} \sin \frac{k_1}{2} & \frac{1}{2}(1 - e^{ik_1}) \\ \frac{1}{2}(1 - e^{-ik_1}) & \sin \frac{k_1}{2} \end{pmatrix}. \quad (\text{B13})$$

Another normalized solution with respect to ε_- , i.e., state localized at the last layer, is $u' = \frac{1}{\sqrt{2}} \left(1, e^{-i \frac{k_1 + \pi}{2}} \right)^\text{T}$. Taking two edge states together, the effective Hamiltonian is

$$H'_{\text{eff}} = \varepsilon_+ uu^\dagger + \varepsilon_- u' u'^\dagger = \frac{1}{2} \begin{pmatrix} 0 & 1 - e^{ik_1} \\ 1 - e^{-ik_1} & 0 \end{pmatrix} \quad (\text{B14})$$

It's very interesting that H'_{eff} is equivalent to the Su-Schrieffer-Heeger model.

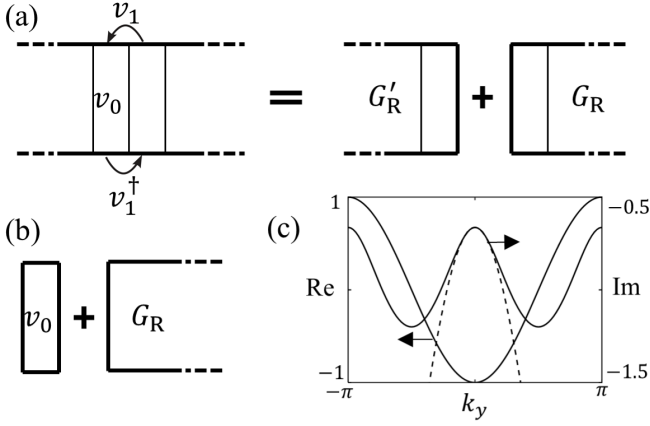


FIG. 7. (a) A full Green's function can be constructed by combining two surface Green's function. (b) The semi-infinite reservoir does not change upon adding another block v_0 . (c) Self-energy of the square lattice (solid lines). $\lambda_1 = 1$, $\lambda_2 = 1.2$ and $\mu = \varepsilon = 0$, hence $\text{Re}(\Sigma) = -\cos k_y$ and $\text{Im}(\Sigma) \approx 1.46 \cos k_y - 2.12$ around $k_y = 0$ (dash line)

Appendix C: Self-energy

The formal expression to evaluate the self-energy is $\Sigma = WG_RW^\dagger$, where G_R represents the surface Green's function and W is the coupling between the closed system and the reservoir. A stable algorithm based on the Schur decomposition (as well as the conventional method using the eigendecomposition) to calculate G_R can be found in Ref. [46]. Here, we follow the procedure using the transfer matrix [47].

Constructing blocks from the reservoir lattice, so that the system is periodic in those blocks v_0 and the hopping v_1 between them is restricted to the nearest neighbor, as shown in Fig. 7a. In terms of those blocks, we have the recursion relation of subblock matrix of the Green's function

$$g_{n+1} = v_1^{-1}(\varepsilon - v_0)g_n - v_1^{-1}v_1^\dagger g_{n-1}, \quad (\text{C1})$$

which can be rewritten as

$$\begin{pmatrix} g_{n+1} \\ g_n \end{pmatrix} = \begin{pmatrix} v_1^{-1}(\varepsilon - v_0) & -v_1^{-1}v_1^\dagger \\ I & 0 \end{pmatrix} \begin{pmatrix} g_n \\ g_{n-1} \end{pmatrix} \equiv \text{T} \begin{pmatrix} g_n \\ g_{n-1} \end{pmatrix}. \quad (\text{C2})$$

The above expression requires v_1 is nonsingular. If it is singular, refer to Ref. [44]. Then surface Green's function is obtained from

$$G_R = [\varepsilon - v_0 - v_1 \mathcal{S}_2 \mathcal{S}_1^{-1}]^{-1} \quad (\text{C3})$$

or

$$G'_R = [\varepsilon - v_0 - v_1^\dagger \mathcal{S}_3 \mathcal{S}_4^{-1}]^{-1}. \quad (\text{C4})$$

G_R or G'_R depends on which semi-infinite part one is interested in (Fig. 7a). $\mathcal{S}_i, i = 1, 2, 3, 4$ is the subblock of

the matrix whose column vectors are ordered eigenvectors of T , i.e.,

$$\begin{pmatrix} \mathcal{S}_2 & \mathcal{S}_4 \\ \mathcal{S}_1 & \mathcal{S}_3 \end{pmatrix}^{-1} \text{T} \begin{pmatrix} \mathcal{S}_2 & \mathcal{S}_4 \\ \mathcal{S}_1 & \mathcal{S}_3 \end{pmatrix} = \begin{pmatrix} \rho_1 & \\ & \dots \end{pmatrix}. \quad (\text{C5})$$

$(\mathcal{S}_2, \mathcal{S}_1)^\text{T}$ corresponds to the eigenvalue $\rho_1 < 1$ and $(\mathcal{S}_4, \mathcal{S}_3)^\text{T}$ corresponds to the eigenvalue $\rho_1 > 1$ respectively. In general, they are not independent and are related by a symmetry (e.g., inversion symmetry).

The self-energy Σ has a very simple form if one notices the semi-infinite reservoir does not change upon adding another block v_0 . With Σ , the Green's function on the additional block is

$$G_R = (\varepsilon - v_0 + \Sigma)^{-1}. \quad (\text{C6})$$

Compare with Eq. C3, we have $\Sigma = -v_1 \mathcal{S}_2 \mathcal{S}_1^{-1}$.

For the lattice Hamiltonian $\mathcal{H}_{\text{Cond}}$ in Eq. 2, $v_0 = 2\lambda_2 \cos k_y + \mu$, $v_1 = \lambda_1$, so

$$\Sigma = -\frac{1}{2\lambda_1}(\Lambda + \sqrt{-4\lambda_1^2 + \Lambda^2}) \quad (\text{C7})$$

with $\Lambda = \mu - \varepsilon + 2\lambda_2 \cos k_y$.

Appendix D: Response profile

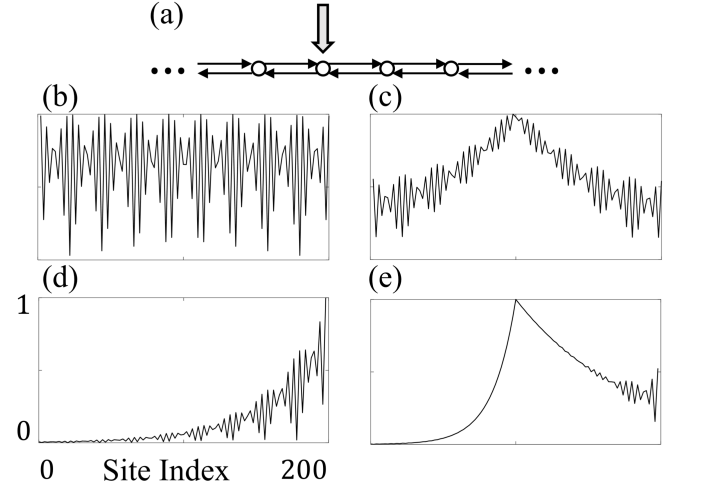


FIG. 8. Response profile corresponding to a unit impulse (Dirac delta function, $E = 0.279$). (a) Hatano-Nelson model. (b) Hermitian case. (c) NH case with global dissipation. (d) Pseudo-Hermitian case. (e) NH case under skin effect and global dissipation.

Here, we give some simple examples to illustrate the response profile, which is an indicator of non-Bloch transport. The model is the Hatano-Nelson model under the open boundary condition:

$$\mathcal{H}_{\text{HN}} = \sum_i \left[t e^{i\vartheta} a_i^\dagger a_{i+1} + t e^{-i\vartheta} a_{i+1}^\dagger a_i - i\mu a_i^\dagger a_i \right], \quad (\text{D1})$$

where we add the global complex onsite potentials μ . Henceforth we set the nearest neighbor hopping t parameter to unity.

- Hermitian case: $\vartheta = \frac{\pi}{2}$ and $\mu = 0$. The response profile corresponding to a excitation is shown in Fig. 8b, and the excited Bloch wave propagates without attenuation.
- NH case with a global dissipation: $\vartheta = \frac{\pi}{2}$ and $\mu = 0.05$, the eigenvalues of \mathcal{H}_{HN} are in the complex domain owing to μ , but μ does not lead to NH skin effect. As shown in Fig. 8c, the attenuation shows no inclination to the propagation orientation, thus the response profile corresponding to a excitation is $\propto \begin{cases} e^{\beta y}, & y < 0 \\ e^{-\beta y}, & y > 0 \end{cases}, \beta \in \mathbb{R}$, which consists with our intuition of wave attenuation owing to the loss.
- Pseudo-Hermitian case with skin effect: $\vartheta = \frac{\pi}{2} + 0.05i$ and $\mu = 0$, the eigenvalues of \mathcal{H}_{HN} are all real numbers due to pseudo-Hermiticity $\eta^{-1}\mathcal{H}_{\text{HN}}\eta = \mathcal{H}_{\text{HN}}$. The eigenstates pile up at the boundary, exhibiting NH skin effect. The response profile corresponding to a unit excitation is shown in Fig. 8d, and the profile $\propto e^{\alpha y}, \alpha \in \mathbb{R}$ because of the skin effect.
- NH case with both the skin effect and the global dissipation: $\vartheta = \frac{\pi}{2} + 0.05i$ and $\mu = 0.15$. Figure 8e shows the calculated response profile, which is roughly $\sim \begin{cases} e^{(\alpha+\beta)y}, & y < 0 \\ e^{(\alpha-\beta)y}, & y > 0 \end{cases}$. The decay (or growth) rate is orientation-dependent under the competition between skin effect and global dissipation.

Figure 9 shows some calculated results of the effective chain model (see text around Eq. 5 in the main text).

Appendix E: Realization of the hopping with a phase

Our previous works [25, 26] develop a correspondence between circuit networks and tight-binding lattice models. We want to apply this theory to higher-frequency regions, such as radio and optical frequencies. Higher frequencies imply decreasing wavelengths. This follows that voltages and currents no longer remain spatially uniform when compared to the geometric size of the discrete circuit elements. As a consequence, they have to be treated as propagating waves. Since Kirchhoff's voltage and current laws do not account for these spatial variations, we must significantly adjust the analysis from conventional lumped to distributed circuit representation.

Multiple port networks are essential tools in restructuring and simplifying complicated circuits as well as in providing key insight into the performance of devices. To describe such network input-output parameter relations,

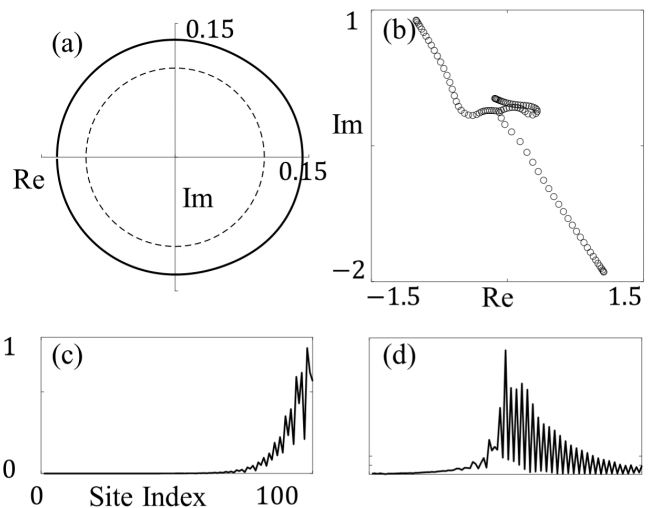


FIG. 9. Calculated results of the effective chain model. (a) Generalized Brillouin zone. In plotting, we use $(|\beta| - 0.99)e^{i\text{Arg}(\beta)}$, $\beta = e^{i\tilde{k}}$ in which \tilde{k} is the complex wave number. (b) Eigenvalues of the chain Hamiltonian with open boundaries. (c) Eigenvector with respect to the eigenvalue $E = 0$. (d) Response profile corresponding to a unit impulse ($E = 0.028$)

we have impedance, admittance, S-parameter, hybrid, and ABCD parameters—conversions exist between these sets. However, some relations may not be well-defined, such as the admittance of a circulator (see subsection 1), causing difficulty in finding the correspondence between higher-frequency networks and tight-binding lattice models. The principal advances of the S-parameter are that: (i) it is always well-defined in a passive device; (ii) the experimental determination of it is convenient without the need to know the internal structure of the device. Here, we show how to realize the hopping with a phase (we set the coupling amplitude to unity) in the TTC network by designing the S-parameter (see subsection 2-4) when the admittance of the device is not available. The phased-hopping breaks the reciprocity, i.e., $t_{ij} \neq t_{ji}$, so we use a circulator to realize this hopping. The ‘black box’ treatment of the S-parameter indicates that distinct devices or different network configurations can realize the same phased-hopping since they may have an identical S-parameter (see subsection 4). The calculation of S-parameters is based on the signal flow graph, subsection 2 will provide some context.

1. Ill-defined admittance of microwave circulators

The circulator geometry (Fig. 10a) can readily be analyzed using the lumped element configuration (Fig. 10b illustrates the network). The usual arrangement consists of a ferrite disk with three strips wound on it: i) the strips are oriented at 120° with respect to each other and are electrically short at the end of them; ii) a direct magnetic

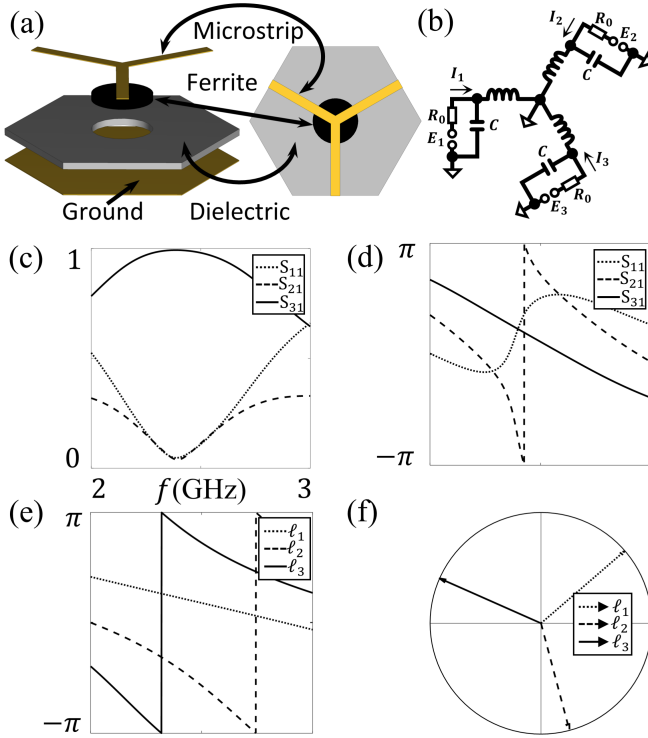


FIG. 10. (a) Schematic of a three-port microstrip circulator. (b) Shunt network of lumped element circulator. (c) and (d) Scattering parameters (amplitude and phase) of the circulator from CST simulation. (e) Characteristics (ℓ_1, ℓ_2, ℓ_3) as function as the frequency varies, the circulator resonates at 2.4 GHz. (f) Eigenvalues of the scattering matrix at 2.4 GHz, $u^{-1}Su = \text{diag}(e^{i\ell_1}, e^{i\ell_2}, e^{i\ell_3})$, where $(\ell_1, \ell_2, \ell_3) = (\ell_0, \ell_0 + \frac{2\pi}{3}, \ell_0 - \frac{2\pi}{3})$ and $\ell_0 \approx 0.71$.

field H_0 is applied normal to the plane of the circulator, so the relative permeability tensor μ_{ij} of the ferrite disk is

$$[\mu_{ij}] = \begin{pmatrix} \mu & -i\kappa & 0 \\ i\kappa & \mu & 0 \\ 0 & 0 & 1 \end{pmatrix}. \quad (\text{E1})$$

with

$$\begin{aligned} \mu &= 1 + \frac{\omega_0 \omega_m}{\omega_0^2 - \omega^2}, \\ \kappa &= \frac{\omega \omega_m}{\omega^2 - \omega_0^2}. \end{aligned} \quad (\text{E2})$$

$\omega_0 = \gamma(H_0 - N_z M_s)$, and $\omega_m = \gamma M_s$, where M_s is the saturation magnetization, γ is the gyromagnetic ratio, N_z is the demagnetizing factor. The presence of imaginary off-diagonal components having opposite signs in μ_{ij} is the basis for the nonreciprocal effect.

The energy within the disk is essentially magnetic because of shorted strips. That follows that the simplified equivalent circuit in the disk, which retains all of the electrical characteristics, contains three mutual inductances. Shunt capacities out of the disk are added

to maintain the characteristic impedance. So, the voltage-current relationships (impedance) at the terminals of the disk structure are

$$\begin{pmatrix} V_1 \\ V_2 \\ V_3 \end{pmatrix} = i\omega L_0 \begin{pmatrix} \mu & \frac{i\kappa - \mu}{2} & \frac{-i\kappa - \mu}{2} \\ \frac{-i\kappa - \mu}{2} & \mu & \frac{i\kappa - \mu}{2} \\ \frac{i\kappa - \mu}{2} & \frac{-i\kappa - \mu}{2} & \mu \end{pmatrix} \begin{pmatrix} I_1 \\ I_2 \\ I_3 \end{pmatrix} \equiv Z \begin{pmatrix} I_1 \\ I_2 \\ I_3 \end{pmatrix}. \quad (\text{E3})$$

Note that $Z \neq Z^T$ as $\mu_{ij} \neq \mu_{ji}$.

The admittance of the circulator, which is the inverse of Z , is ill-defined since its impedance Z is singular (i.e., the voltages do not determine the currents). Nevertheless, we can calculate the pseudoinverse of Z ,

$$Z^+ = \frac{4\mu}{3(-\kappa^2 + 3\mu^2)} \frac{1}{i\omega L_0} \begin{pmatrix} \mu & \frac{-i\kappa - \mu}{2} & \frac{i\kappa - \mu}{2} \\ \frac{i\kappa - \mu}{2} & \mu & \frac{-i\kappa - \mu}{2} \\ \frac{-i\kappa - \mu}{2} & \frac{i\kappa - \mu}{2} & \mu \end{pmatrix}. \quad (\text{E4})$$

One can hardly find any correspondence to \mathcal{H}_Δ .

The scattering matrix S however is well-defined (note that every passive circuit has a scattering matrix [48]), and $SS^\dagger = 1$ if the network is dissipationless. The circulator respects C3 symmetry, thus we can use the frame u defined in the main text to diagonalize the matrix, $u^{-1}Su = \text{diag}(e^{i\ell_1}, e^{i\ell_2}, e^{i\ell_3})$. This also follows that $S_{11} = S_{22} = S_{33}$, $S_{12} = S_{23} = S_{31}$ and $S_{21} = S_{32} = S_{13}$. Similarly, the eigenvalues uniquely define the scattering relation between ports.

Figure 10c and d show the scattering parameters of the circulator and its characteristics as frequency varies. At the resonant frequency of the circulator, the scattering matrix is approximate to an ideal circulator:

$$S_{\text{id}} = e^{i\ell_0} \begin{pmatrix} 0 & 0 & 1 \\ 1 & 0 & 0 \\ 0 & 1 & 0 \end{pmatrix}, \quad (\text{E5})$$

and the characteristics are $(\ell_1, \ell_2, \ell_3) = (\ell_0, \ell_0 + \frac{2\pi}{3}, \ell_0 - \frac{2\pi}{3})$.

2. Review of signal flow graphs

The analysis of networks is greatly facilitated through signal flow graphs. The primary components of the graph are nodes and branches. Each port i of a network has two nodes: node a_i is deployed to identify a entering wave, while b_i a reflected wave. A branch is a directed path between two nodes representing signal flow from one node to another. The S-parameter (the scattering matrix, e.g., Fig. 11a and b) is defined as

$$\begin{aligned} S_{ii} &= \left. \frac{b_i}{a_i} \right|_{a_{j \neq i} = 0}, \\ S_{ji} &= \left. \frac{b_j}{a_i} \right|_{a_{l \neq i} = 0}. \end{aligned} \quad (\text{E6})$$

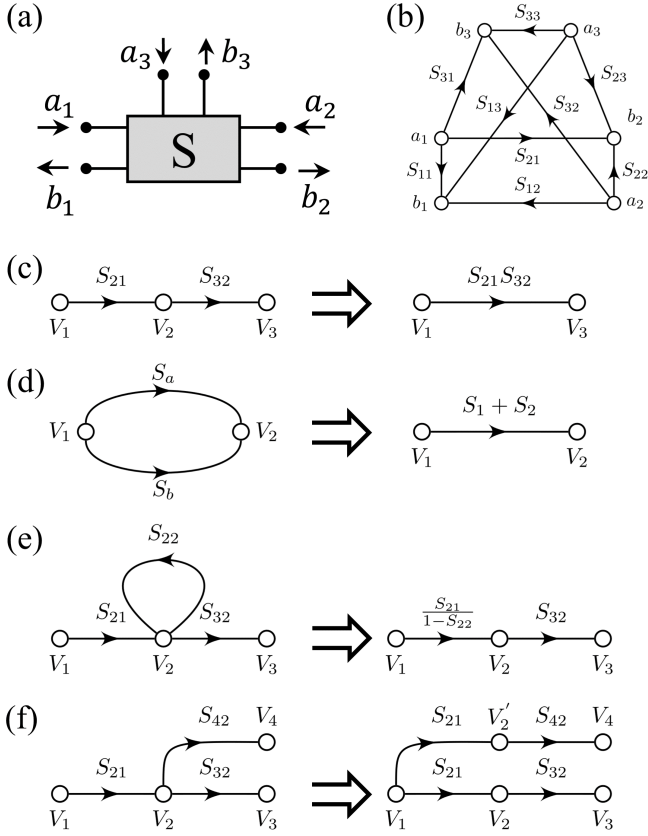


FIG. 11. The signal flow graph representation of a three-port network and decomposition rules of flow graph. (a) A general three-port network and (b) its signal flow graph. Decomposition rules: (c) Series rule, (d) Parallel rule, (e) Self-loop rule, (f) Splitting rule.

In the network, we use the normalized incident power wave a_i and reflected power wave b_i :

$$\begin{aligned} a_i &= \frac{1}{2\sqrt{Z_0}}(V_n + Z_0 I_n), \\ b_i &= \frac{1}{2\sqrt{Z_0}}(V_n - Z_0 I_n), \end{aligned} \quad (\text{E7})$$

where the Z_0 is the characteristic impedance of the connecting waveguide on the input and output side of the network. In what follows, we set $Z_0 = 1$ for simplicity. A signal flow graph can be reduced to a single branch between two nodes using the four basic decomposition rules to obtain any desired wave amplitude ratio (Fig. 11c-f).

3. Two sites

We employ a three-port ideal circulator (we set $\ell_0 = 0$ in Eq. E5) to realize the two-site coupling with an arbitrary phase θ and set the coupling amplitude to unity.

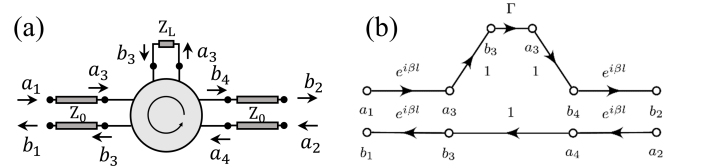


FIG. 12. Realization of two-site hopping with a phase. (a) Schematic of the realization. (b) Corresponding flow graph.

The Hamiltonian of the two sites reads

$$\mathcal{H}_2 = \begin{pmatrix} & e^{i\theta} \\ e^{-i\theta} & \end{pmatrix}. \quad (\text{E8})$$

The bilinear transform $\frac{i+\mathcal{H}_2}{i-\mathcal{H}_2}$ gives $\begin{pmatrix} & e^{i(\theta-\frac{\pi}{2})} \\ e^{i(\frac{\pi}{2}-\theta)} & \end{pmatrix}$. One can not find a θ -independent frame that diagonalizes the transformed matrix, but we can define two characteristics χ_{\pm} as $\chi_{\pm} = \pm(\theta - \frac{\pi}{2})$ by noting the off-diagonal form of the transformed matrix.

Two ports of the circulator are attached to the waveguides with electrical length βl , where β is the wavenumber in the waveguide and l is the physical length of the waveguide, and the rest port is terminated in a load impedance Z_L . Using the flow graph Fig. 12b, the S-parameter of this configuration is

$$S_2 = \begin{pmatrix} & e^{2i\beta l} \\ \Gamma e^{2i\beta l} & \end{pmatrix}, \quad (\text{E9})$$

where $\Gamma = \frac{Z_L - Z_0}{Z_L + Z_0}$ is the reflection coefficient. Unitary matrix $S_2 S_2^\dagger = 1$ leads to $|\Gamma| = 1$. Similarly, we can define the characteristics of S_2 as $\ell_+ = 2\beta l$ and $\ell_- = \text{Arg}(\Gamma) + 2\beta l$. χ_{\pm} and ℓ_{\pm} give us the correspondence, for example, when $\theta = \frac{\pi}{2}$, $\beta l = 0$, $Z_L = 0$. Note that the load Z_L can be realized by a piece of waveguide with its end grounded or open (see Fig. 16 and text around there).

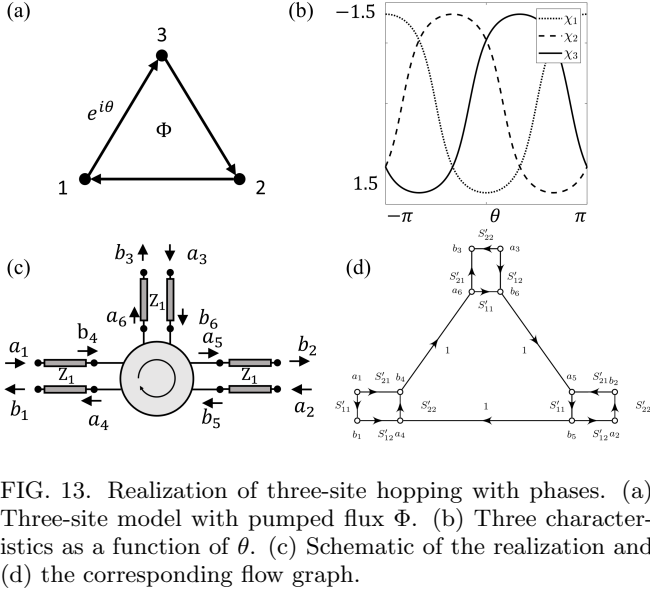
4. Three sites

Here, we show how to realize the next-nearest neighbor hopping required in the Haldane model. To illustrate it, consider the following three-site Hamiltonian (Fig. 13a):

$$\mathcal{H}_\Delta = \begin{pmatrix} 0 & e^{i\theta} & e^{-i\theta} \\ e^{-i\theta} & 0 & e^{i\theta} \\ e^{i\theta} & e^{-i\theta} & 0 \end{pmatrix}. \quad (\text{E10})$$

The transformed matrix $\mathcal{S} = \frac{i+\mathcal{H}_\Delta}{i-\mathcal{H}_\Delta}$ can be diagonalized by the frame \mathbf{u} because of the C3h symmetry: $\mathbf{u}^{-1} \mathcal{S} \mathbf{u} = \text{diag}(e^{i\chi_1}, e^{i\chi_2}, e^{i\chi_3})$, where $\mathbf{u} = (\mathbf{v}_1, \mathbf{v}_2, \mathbf{v}_3)$, $\mathbf{v}_1 = (1, 1, 1)^T$, $\mathbf{v}_2 = (1, \alpha, \alpha^2)^T$, $\mathbf{v}_3 = (1, \alpha^2, \alpha)^T$ with $\alpha = e^{\frac{2\pi i}{3}}$. The characteristics are shown in Fig. 13b as θ varies.

To realize that, we employ a three-port circulator with its ports attached to waveguides, see Fig. 13c. The



waveguides attached have the characteristic impedance of Z_1 , and the electrical length is $\beta_1 l_1$. Using the flow graph Fig. 13d, the S-parameter of this configuration is

$$\begin{aligned} S_{11} &= \frac{a(a^3 - ab^2 - 1)}{a^3 - 1} \\ S_{12} &= \frac{-ab^2}{a^3 - 1} \\ S_{21} &= \frac{-b^2}{a^3 - 1}, \end{aligned} \quad (\text{E11})$$

and $S_{11} = S_{22} = S_{33}$, $S_{12} = S_{23} = S_{31}$ and $S_{21} = S_{32} = S_{13}$ due to C_3 symmetry of the configuration (i.e. S is a circular matrix denoted as $S = \text{circ}(S_{11}, S_{12}, S_{13})$). $S' = \begin{pmatrix} a & b \\ b & a \end{pmatrix}$ is the scattering matrix because of the impedance mismatch between connecting waveguides of Z_0 and attached waveguides of Z_1 , $a = e^{i\beta_1 l_1} \frac{Z_0 - Z_1}{Z_0 + Z_1}$. The mirror symmetry of the impedance-mismatch scattering leads to $S'_{12} = S'_{21}$ and $a^2 + b^2 = 1$ follows from $S' S'^{\dagger} = 1$. The characteristics of S-parameter $\ell_{1,2,3}$ (i.e., the eigenvalues of the S-parameter) and characteristics of transformed-matrix $\chi_{1,2,3}$ give the correspondence, for example, when $\theta = \frac{\pi}{2}$, $\beta_1 l_1 = 0$, $Z_1 = Z_0$.

What is unique to the three-port ideal circulator is that we can calculate its admittance through $Y_{\text{id}} = \frac{1 - S_{\text{id}}}{1 + S_{\text{id}}}$ (set $\ell_0 = 0$). An alternative approach to calculating this diagram structure (Fig. 13a) using the Kirchhoff's law can be found around Eq. F13.

5. Four sites

Here, we show how to introduce the flux through a four-site plaquette. Without losing generality, we set the coupling amplitude to be unity and the onsite potential

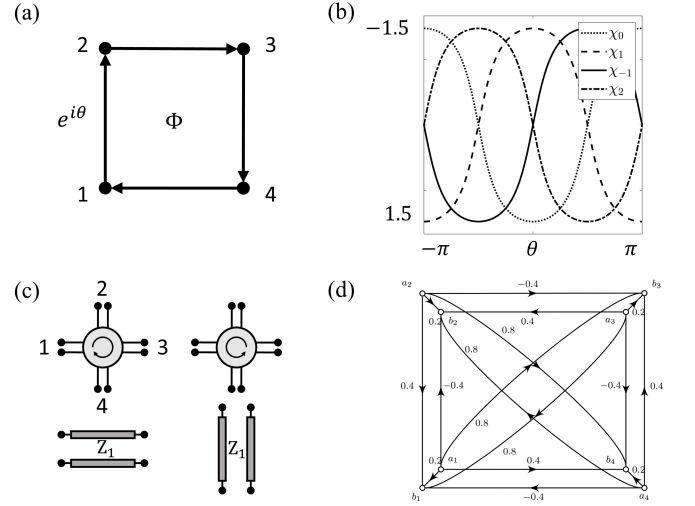


FIG. 14. Realization of four-site hopping with phases. (a) Four-site model with pumped flux Φ . (b) Four characteristics as a function of θ . (c) Schematic of the realization by the channel decomposition and (d) the corresponding flow graph.

to be zero (Fig. 14a). The resulting Hamiltonian is

$$\mathcal{H}_{\square} = \begin{pmatrix} 0 & e^{i\theta} & 0 & e^{-i\theta} \\ e^{-i\theta} & 0 & e^{i\theta} & 0 \\ 0 & e^{-i\theta} & 0 & e^{i\theta} \\ e^{i\theta} & 0 & e^{-i\theta} & 0 \end{pmatrix}. \quad (\text{E12})$$

When $\Phi = 0$, the model respects D4h symmetry, So according to group theory, we can generate the equivalence representation (i.e., transform between equivalent sites) for the symmetry. In this case, the equivalence representation Γ is reducible:

$$\Gamma = A_1 \oplus B_1 \oplus E \quad (\text{E13})$$

where A_1 , B_1 and E denote the unreducible representation of D4h. E is a 2-by-2 matrix, meaning that two of the four eigenvalues of \mathcal{H}_{\square} are degenerate. Those two-fold eigenvalues can be lifted by pumping flux Φ , and \mathcal{H}_{\square} respects C_4 symmetry when pumping. So we can use a symmetrical set of basis

$$u = \begin{pmatrix} 1 & 1 & 1 & 1 \\ 1 & -1 & i & -i \\ 1 & 1 & -1 & -1 \\ 1 & -1 & -i & i \end{pmatrix}. \quad (\text{E14})$$

Under this frame u , the transformed matrix $S = \frac{i + \mathcal{H}_{\square}}{i - \mathcal{H}_{\square}}$ can be diagonalized as $u^{-1} S u = \text{diag}(e^{i\chi_0}, e^{i\chi_1}, e^{i\chi_{-1}}, e^{i\chi_2})$. Those characteristics are shown in Fig. 14b as θ varies.

One of the simplest ways to realize \mathcal{H}_{\square} is by taking advantage of two-site coupling (see text around Eq. E8). Here, we introduce the other two ways. Without losing generality, we set $\theta = \frac{\pi}{2}$ in the following.

I —If the S-parameter shares the same characteristics as \mathcal{S} , S will take the form

$S = \mathbf{u} \cdot \text{diag}(e^{i\chi_0}, e^{i\chi_1}, e^{i\chi_2}, e^{i\chi_3}) \cdot \mathbf{u}^{-1}$. $S = \text{circ}(0.2, -0.4, 0.8, 0.4)$ when $\theta = \frac{\pi}{2}$. We can decompose S into several channels, $S = S_{\circlearrowleft} + S_{\circlearrowright} + S_{\nearrow} + S_{\searrow}$ where $S_{\circlearrowleft} = -0.4 \cdot \text{circ}(0, 1, 0, 0)$, $S_{\circlearrowright} = 0.4 \cdot \text{circ}(0, 0, 0, 1)$,

$$S_{\nearrow} = \begin{pmatrix} 0.2 & 0.8 \\ 0.8 & 0.2 \end{pmatrix} \text{ and } S_{\searrow} = \begin{pmatrix} 0.2 & 0.8 \\ 0.8 & 0.2 \end{pmatrix}. \quad (\text{E15})$$

By inspection, we find that S_{\circlearrowleft} and S_{\circlearrowright} are nothing but the S-parameters of four-port right-hand and left-hand circulators. S_{\nearrow} or S_{\searrow} corresponds to the reciprocal scattering between port-1 and port-3 or scattering between port-2 and port-4 (Fig. 14c). This construction can be easily verified by the signal flow graph shown in Fig. 14d.

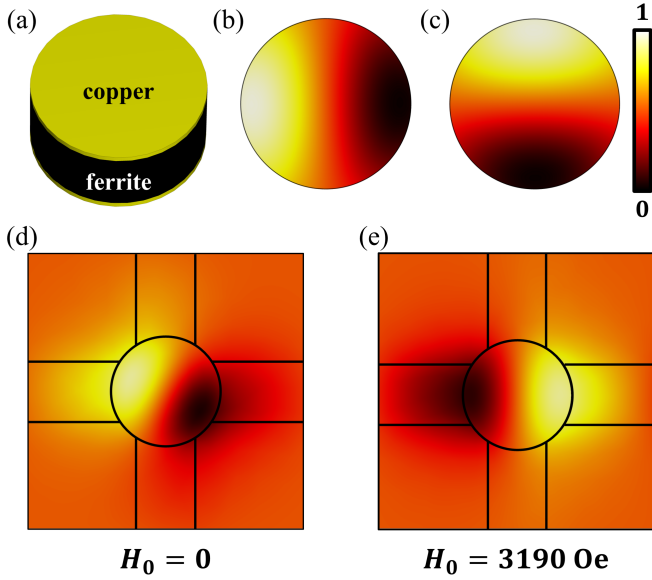


FIG. 15. Realization of Four-site hopping by the ferrite eigenvalue adjustment. (a) Geometry of a dielectric disk. (b) and (c) Field patterns of $\text{HE}_{\pm 1,1,1}$. (d) Scattering field distribution without external magnetic field. (e) Scattering field distribution under external magnetic field. More parameters see the caption of Fig. 4 in the main text.

II— The above realization is still cumbersome for experiments. The construction discussed here is based on the ferrite eigenvalue adjustment for the 4-port nonreciprocal devices [49–51]. The geometry of a dielectric disk is shown in Fig. 15a. Here, we focus on the resonant modes $\text{HE}_{\pm 1,1,1}$ supported by the disk. Without the external magnetic field, two modes are degenerate due to the cylinder symmetry of the disk, and their field patterns resemble the p_x and p_y orbitals of an atom (Fig. 15b and c). If we attach four ports to this disk under the C_4 symmetry (e.g., inset of Fig. 4b in the main text), the S-parameter between ports around the $\text{HE}_{\pm 1,1,1}$ eigenfrequency is $S = \text{circ}(0, 0, 1, 0)$. This follows that the excitation from one port only excites one mode of $\text{HE}_{\pm 1,1,1}$. For example, excitation from port 1 can only excite $\text{HE}_{1,1,1}$

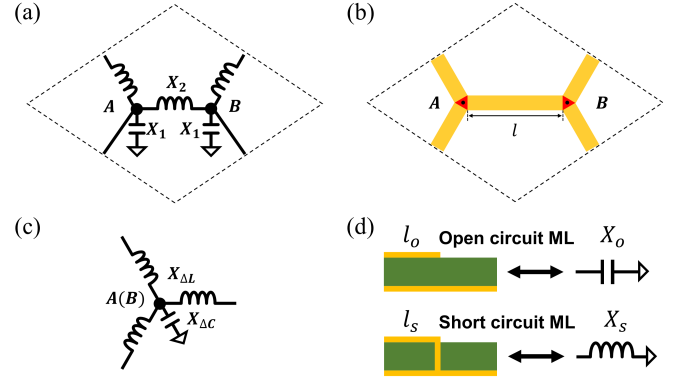


FIG. 16. (a) Unit cell of the circuit graphene lattice. (b) Unit cell of ML graphene lattice. (c) The equivalent circuit of a red triangle part in (b). (d) The equivalent circuits of open and short circuit ML.

mode, so it only couples to port 3, and there is no cross-over between channel $1 \leftrightarrow 3$ and channel $2 \leftrightarrow 4$ (Fig. 15d).

Correspondingly, the characteristics of $\text{circ}(0, 0, 1, 0)$ are $(\ell_0, \ell_1, \ell_{-1}, \ell_2) = (0, \pi, \pi, 0)$ (Fig. 4b left in the main text), $\ell_+ = \ell_-$ because of the D_{4h} symmetry, $\ell_1 = \ell_2$ because of the accidental degeneracy. Those characteristics can be adjusted by the amplitude of the direct magnetic field. This adjustment rotates the standing wave formed by $\text{HE}_{1,1,1}$ to make sure $\ell_{\pm 1} = \pm 0.7048\pi$ (Fig. 15e), and it lifts the degeneracy of ℓ_1 and ℓ_{-1} without affecting ℓ_0 and ℓ_2 (Fig. 4b right in the main text).

Appendix F: Simulations of microstrip line metamaterials

This section gives the details about simulations of the metamaterials. Firstly, we use microstrip line (ML) to demonstrate the flexibility of TTCs to upgrade to higher frequencies. The ML circuit also exhibits the property of momentum resolution, which is the advantage of TTCs. Moreover, in order to construct Haldane model with ML, we analyze the admittance properties of a circulator.

1. Upgrade of TTCs

To construct the topological junction, we first consider the graphene lattice with only the nearest neighbor hopping t_1 and onsite potential μ , which is the basis of the Haldane model. The Hamiltonian of such lattice reads

$$\mathcal{H}_{\text{Gra}} = t_1 \sum_{(i,j)} c_i^\dagger c_j + \mu \sum_i c_i^\dagger c_i \quad (\text{F1})$$

and can be realized with temporal topolelectrical circuits (TTCs). The unit cell of the corresponding circuit lattice is shown in Fig. 16a. The distance between the sublattices A and B is set to be 1. Thus, the lattice constant is

$\sqrt{3}$ and the admittance matrix J_{Gra} in momentum space reads

$$J_{\text{Gra}} = -\frac{1}{i\omega L_1} \begin{pmatrix} 0 & J_{12} \\ J_{12}^\dagger & 0 \end{pmatrix} + \left(\frac{3}{i\omega L_1} + i\omega C_1 \right) \mathbb{I}_2$$

$$J_{12} = 1 + e^{\frac{i}{2}(\sqrt{3}k_x + 3k_y)} + e^{\frac{i}{2}(-\sqrt{3}k_x + 3k_y)}, \quad (\text{F2})$$

where ω is the operating angular frequency and \mathbb{I}_n is the n -by- n identity matrix. Generally, the nearest neighbor hopping t_1 is realized with the inductor L_1 and the onsite potential is adjusted through the grounded capacitor C_1 .

As stated in the main text, TTCs can be upgraded to the microwave domain. Such upgrade is practical for many platforms, e.g., waveguide, coaxial line, ML and so on, and we use ML to illustrate the procedure. ML consists of a dielectric substrate with a conductor strip attached to its surface and the ground plane on the other. Under a certain parameter range, the electromagnetic properties of an ML with width w and length l are equivalent to a pi-shaped circuit as shown in Fig. 2a and 2b. The admittances of the components are

$$X_1 = i\omega C_{\text{ML}} = i\frac{1}{Z_0} \tan \frac{k_0 l}{2},$$

$$X_2 = \frac{1}{i\omega L_{\text{ML}}} = -i\frac{1}{Z_0 \sin k_0 l}, \quad (\text{F3})$$

where Z_0 is the characteristic impedance and $k_0 = 2\pi/\lambda_0$ is the wave number. The ML parameters are $w = 2.1$ mm, $t = 35$ μm , $l = 16.7$ mm, $h = 1.2$ mm, $\epsilon_r = 4.6$, $f = 2.4$ GHz, which lead to the impedance $Z_0 = 50$ Ω and the electrical length $k_0 l = \frac{\pi}{2}$. Thus, $X_1 + X_2 = 0$, the self-admittance of both site A and B is equal to 0.

Because of the equivalence, the circuit cell of Fig. 16a can be replaced by ML as shown in Fig. 16b. Such connection creates additional regions as the red triangles in Fig. 16b, which introduce additional electrical lengths. Figure 16c is the equivalent circuit of a triangle, and the element parameters can be exactly calculated. However, for simplicity, we can take the influence into account from the view of wave propagation, for which the commercial simulator CST studio is used. When transmitting along a length of ML with parameters above, the electromagnetic wave acquires a phase shift of $-k_0 l = -\frac{\pi}{2} = -90^\circ$. Furthermore, the phase shift from one side of the triangle to another is -2.3° . Therefore, we can adjust the length l to 16.2 mm to decrease the electrical length. Then in Fig. 16b, the wave also acquires a phase shift of -90° from site A to B . We construct the ML graphene lattice in CST (Fig. 17a) and simulate the field distribution. A waveguide port is set at P and the field within the green box is simulated at $f = 2.4$ GHz. All boundaries are set as perfect electric conductors.

After Fourier Transform (FT), the energy band section at certain momentum is achieved (Fig. 17b). The theoretical result calculated from Eq. F1 is also given for comparison. As an upgrade of TTCs, the ML lattice also exhibits the property of momentum resolution. Moreover, there are more than one way to adjust the

momentum at which the band section is obtained after FT. For example, according to the equivalence, the self-admittance terms can be easily tuned by altering the operating frequency f . When $f \rightarrow f'$, the corresponding wave number $k_0 \rightarrow k'_0$, and so does the electrical length. Thus, the self-admittance $X_1 + X_2$ of any sublattice site, namely, the onsite potential μ is no longer 0. In addition to the way of altering f , μ can also be adjusted at fixed f by attaching a length of open or short circuit ML to sublattice sites. As shown in Fig. 16d, a length of open (short) circuit ML is equivalent to a grounded capacitor (inductor), whose admittance is

$$X_o = i\frac{1}{Z_0} \tan k_0 l_o,$$

$$X_s = -i\frac{1}{Z_0 \tan k_0 l_s}. \quad (\text{F4})$$

Therefore, attaching a length of ML to a site simply alters the self-admittance of it, adjusting the onsite potential μ . To demonstrate that, simulation at different onsite potentials is caused (Fig. 17c and 17d).

2. ML Haldane model

To make graphene topological, imaginary second-nearest neighbor hopping related with direction is added to break the time-reversal symmetry, which is the Haldane model. For ML lattice, such hopping can be introduced through a circulator (Fig. 18a). The propagation of wave in a circulator depends on the location of the three ports. For an ideal circulator, the S matrix is

$$S_{\text{cir}} = \begin{pmatrix} 0 & 0 & 1 \\ 1 & 0 & 0 \\ 0 & 1 & 0 \end{pmatrix} \quad (\text{F5})$$

and the corresponding admittance matrix is

$$J_{\text{cir}} = \frac{1}{Z_0} \begin{pmatrix} 0 & 1 & -1 \\ -1 & 0 & 1 \\ 1 & -1 & 0 \end{pmatrix} = i\frac{1}{Z_0} \begin{pmatrix} 0 & -i & i \\ i & 0 & -i \\ -i & i & 0 \end{pmatrix}. \quad (\text{F6})$$

However, an actual circulator always carries a phase shift of θ and the corresponding S and admittance matrices are

$$S_{\text{act}} = \begin{pmatrix} 0 & 0 & e^{i\theta} \\ e^{i\theta} & 0 & 0 \\ 0 & e^{i\theta} & 0 \end{pmatrix}, J_{\text{act}} = \frac{\mathbb{I}_3 - S_{\text{act}}}{Z_0(\mathbb{I}_3 + S_{\text{act}})}. \quad (\text{F7})$$

Moreover, connecting circulators to the lattice sites of ML graphene lattice also requires certain lengths of ML. To calculate the overall admittance J'_{cir} introduced by an actual circulator, the schematic is shown as Fig. 18b. I and V are the current and voltage respectively, and l' is the length of the connecting ML. The corresponding admittance X'_1 and X'_2 can be calculated as Eq. F3.

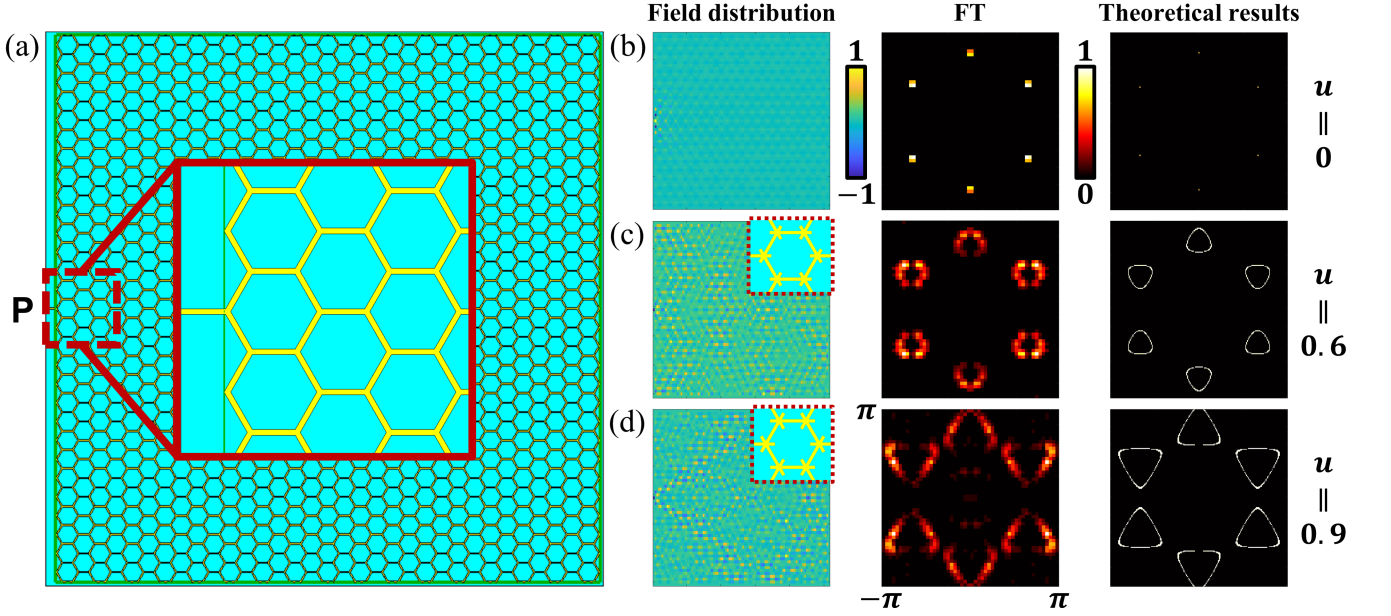


FIG. 17. (a) Simulation model of ML graphene lattice. (b)-(d) Simulated field distributions and the corresponding energy band sections at different onsite potentials. Theoretical results are given for comparison.

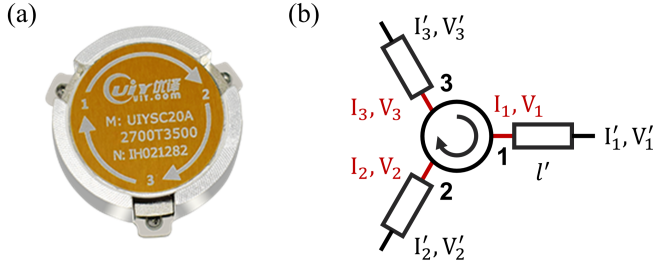


FIG. 18. (a) A circulator. (b) Schematic of connecting a circulator to ML graphene lattice with three lengths of ML.

Denoting $I = [I_1 \ I_2 \ I_3]^T$ and the same for V , I' , and V' , then

$$I' = X'_1 V' + X'_2 (V' - V), \quad (\text{F8})$$

$$X'_2 (V' - V) = X'_1 V + I. \quad (\text{F9})$$

Noting that $I = J_{\text{act}} V$,

$$I' = X'_1 V' + X'_1 V + J'_{\text{cir}} V, \quad (\text{F10})$$

and Eq. F9 can be transformed into

$$V = \left(\frac{X'_1 \mathbb{I}_3 + J_{\text{act}}}{X'_2} + \mathbb{I}_3 \right)^{-1} V'. \quad (\text{F11})$$

Substituting Eq. F11 into Eq. F10,

$$I' = \left(X'_1 + \frac{X'_1 \mathbb{I}_3 + J_{\text{act}}}{\frac{X'_1 \mathbb{I}_3 + J_{\text{act}}}{X'_2} + \mathbb{I}_3} \right) V', \quad (\text{F12})$$

namely

$$J'_{\text{cir}} = X'_1 + \frac{X'_1 \mathbb{I}_3 + J_{\text{act}}}{\frac{X'_1 \mathbb{I}_3 + J_{\text{act}}}{X'_2} + \mathbb{I}_3}. \quad (\text{F13})$$

Introducing the imaginary second-nearest neighbor hopping to the ML graphene lattice with circulators, the Haldane ML lattice with armchair boundaries is constructed as shown in Fig. 19a. The Haldane ML lattice consists of 3 layers. Top layer is the ML graphene lattice with sublattice A and B being connected to circulators at the other 2 layers through vias. The middle and bottom layers are strip line and ML circulators, respectively (the inset of Fig. 19a). Figure 19b shows the corresponding field distribution at $f = 2.4$ GHz, which demonstrates the existence of boundary state. It should be noted that, in simulations, we use microstrip circulators as Fig. 10a and construct a 3-layer model for clarity. While for experimental realization, circulators as Fig. 18a can be used directly to simplify the structure and construct a 2-layer setup.

Appendix G: Kwant simulation

In this section, we firstly introduce the details about simulating the transport of the topological junction with Kwant. Then, in order to realize nearly equivalent scattering properties of a semi-infinite conductor with finite size, the details about imaginary absorbing potential are provided.

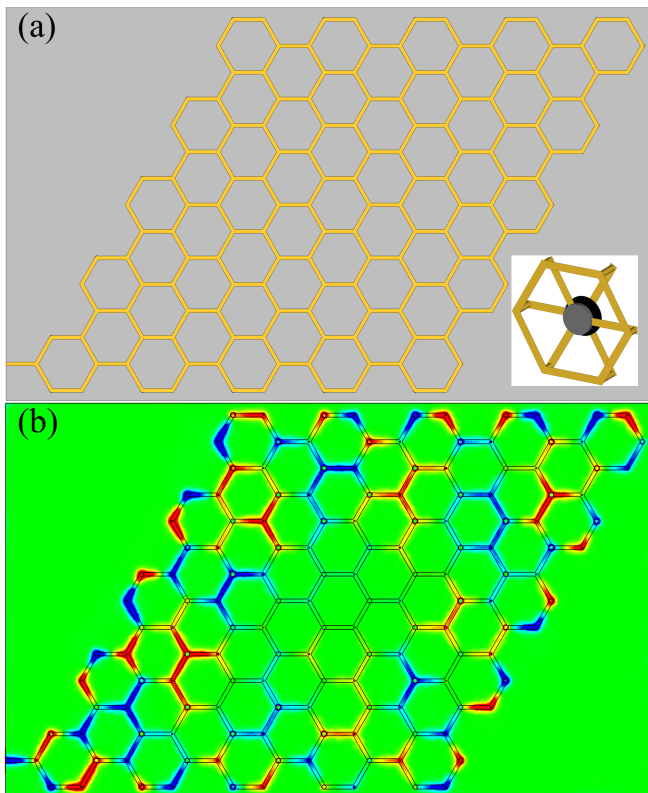


FIG. 19. (a) The simulation model of ML Haldane lattice. (b) Field distribution at $f = 2.4$ GHz.

1. Topological junction

To demonstrate the non-bloch transport of topological insulator-conductor junction, Kwant, an open source Python package, is adopted. Firstly, the simulation model of a Haldane ribbon with armchair boundaries is constructed (Fig. 20a). The corresponding hoppings are set to be $t_1 = t_2 = 1$. Transport properties of the topological insulator are simulated by calculating the Green's function of the upper side for 200 lattice sites. When excited at the 101st site, the response of all sites is depicted as Fig. 20b, which represents for the chiral boundary state of Haldane model. Based on the Haldane ribbon, a semi-infinite conductor with square lattice is attached to sublattice A to construct the topological insulator-conductor junction (Fig. 20c). Hopping parameters of the conductor lattice are set to be $\lambda_0 = \lambda_1 = 1$ and $\lambda_2 = -1.14$. Transport properties of the junction are simulated in the same way and at the same region as above. The corresponding response is shown as Fig. 20d. In Fig. 20b, waves cannot propagate along $-x$ to the left because of the boundary state being clockwise. However, in Fig. 20d, waves decay exponentially at different rates in different directions, which represents for the non-bloch transport and can be attributed to the non-Hermiticity introduced by the Hermitian semi-infinite conductor.

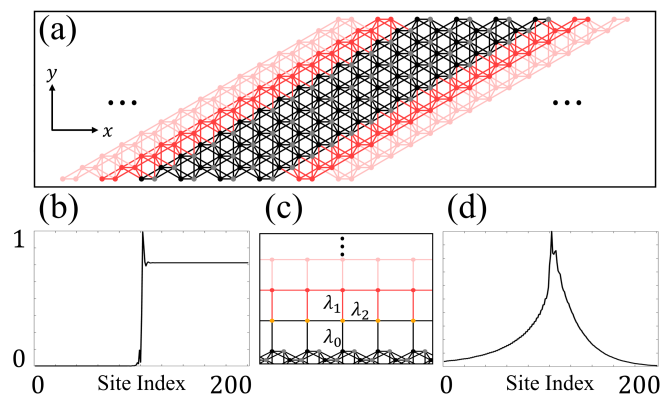


FIG. 20. (a) The Kwant simulation model of Haldane ribbon with armchair boundaries. Black and grey sites represent for sublattice A and B , respectively. Red lattice stands for the infinite extension along both directions of x . (b) Response profile of 200 sites on the upper boundary of (a) when excited at the 101st site. (c) The semi-infinite conductor attached to sublattice A of the Haldane ribbon. λ_0 is the hopping between the bottom of conductor lattice and sublattice A on the upper of Haldane lattice. λ_1 and λ_2 are the hopping within conductor lattice along y and x , respectively. (d) Response profile of the same region and excitation as (b) after the attachment of a semi-infinite conductor.

2. Imaginary absorbing potential

Constructing the topological junction needs for a semi-infinite conductor that is impractical for experimental setup. Therefore, imaginary potential method [52, 53] is adopted on a finite conductor to realize equivalent effects as a semi-infinite one. As shown in Fig. 21a, the method consists of two additional regions. In absorbing region, imaginary onsite potential is introduced to the lattice sites to absorb the waves propagating towards the end. Moreover, a buffer region is used to extend the propagation time of the ineluctable backscattering wave so that it would not influence the transportation of the topological junction in certain simulation time. According to Ref. [52], a polynomial form of imaginary onsite potential is adopted:

$$\Sigma(y) = i(n+1)Ay^n, \quad (G1)$$

where n and A are controlling parameters, and y is the order number counted from the start point of the absorbing region (Fig. 21b). Generally, the values of imaginary potential should be large enough so that the waves can be absorbed within a region as small as possible. However, sharp change of the values from one point to the next causes backscattering that weakens the absorption. Thus, the actual problem is the optimization about controlling parameters n , A , and the length of the buffer and absorbing region in y . To obtain appropriate parameters, a finite square lattice with imaginary onsite potential according to Eq. G1 is constructed in Kwant (Fig. 21b). The number of sites in x is 150 and the length of the

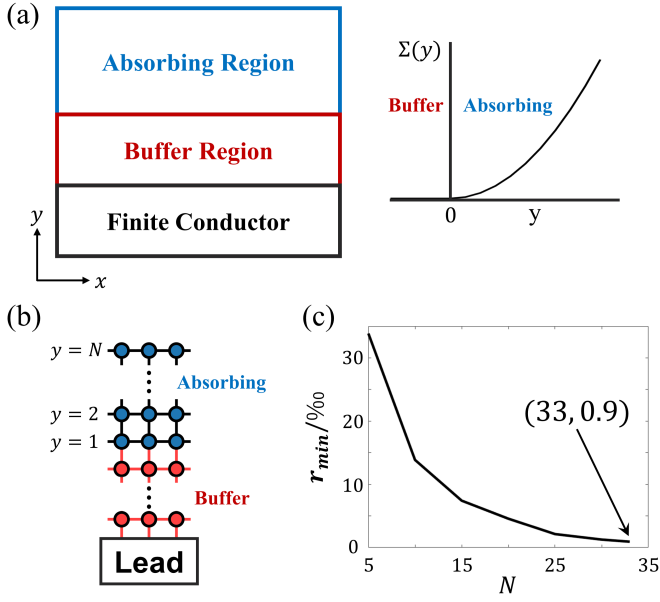


FIG. 21. (a) Schematic of the imaginary potential method. (b) Kwant model used to optimize the controlling parameters. A lead is attached to the bottom to simulate the reflection. (c) The simulated variation of minimum reflectivity r_{min} with the length N of absorbing region in y .

buffer region in y is 20. A lead is attached to the lattice to simulate the reflection. At a fixed length N of the absorbing region, parameter sweep of n and A is performed to minimize the reflection. The same process is executed for different values of N , and the variation of minimum reflectivity r_{min} with N is depicted in Fig. 21c. r_{min} intuitively decreases with the increase of N , and when $N \geq 33$, $r_{min} < 1\%$. Thus, we choose the length of the absorbing region to be 33, and the corresponding controlling parameters for r_{min} are $n = 2.8$ and $A = 6 \times 10^{-6}$.